Journal of CO2 Utilization 57 (2022) 101888

Contents lists available at ScienceDirect

Journal of CO2 Utilization

journal homepage: www.elsevier.com/locate/jcou

# Intrinsic kinetics of $CO_2$ methanation on low-loaded $Ni/Al_2O_3$ catalyst: Mechanism, model discrimination and parameter estimation

Adrián Quindimil [a], Jon A. Onrubia-Calvo [a], Arantxa Davó-Quiñonero [b], Alejandro Bermejo-López [a], Esther Bailón-García [b], Beñat Pereda-Ayo [a], Dolores Lozano-Castelló [b], José A. González-Marcos [a], Agustín Bueno-López [b], Juan R. González-Velasco [a,*]

[a] Department of Chemical Engineering, Faculty of Science and Technology, University of the Basque Country UPV/EHU, Barrio Sarriena, s/n, 48940, Leioa, Bizkaia, Spain

[b] Department of Inorganic Chemistry, University of Alicante, Carretera de San Vicente, s/n, E03080, Alicante, Spain

ARTICLE INFO

*Keywords:*
$CO_2$ methanation
$Ni/Al_2O_3$ catalyst
Kinetic model
Reaction mechanism
H-assisted CO formation route

ABSTRACT

The mechanism and kinetic of $CO_2$ methanation reaction of 9.5 % $Ni/Al_2O_3$ catalyst is analysed under a wide range of operating conditions. Once the catalyst activity is stabilized, the influence of temperature, total pressure and space velocity is studied for kinetic characterisation. A data set comprising of 153 experimental runs has been used to develop a kinetic model capable to accurately predict the reaction rate. $Ni/Al_2O_3$ catalyst shows an apparent activation energy of 80.1 kJ $mol^{-1}$ in $CO_2$ hydrogenation. Data obtained under differential mode adjust quite precisely to a power-law model with $H_2O$ inhibition, with a water adsorption constant of 3.1 $atm^{-1}$ and apparent orders of 0.24 and 0.27 for $H_2$ and $CO_2$, respectively. Based on DRIFTS results, we propose for the first time the H-assisted CO formation route, which is compared with the more conventionally reported carbonyl route, and describe the corresponding reaction rate LHHW equation, resulting in notable improvement for mean deviation ($D$) of 7.0 % in our model related to that based on the carbonyl route ($D$ = 20.1 %) usually suggested for catalysts with higher Ni loads around 20 %. The H-assisted CO formation route considers the formate species decomposition into carbonyls via H-assisted CO formation mechanism and further carbonyls hydrogenation into CHO as the rate determining step. Thus, the LHHW mechanism, in which carbonyls as well as formate species participate in $CO_2$ methanation, is capable to reflect the kinetics of lowly-loaded $Ni/Al_2O_3$ catalyst with high accuracy under relevant process conditions (315−430 °C, 1−6 bar, $H_2$ to $CO_2$ molar ratios between 1–16 and, different reagents and products partial pressures).

## 1. Introduction

The last century has been characterized by exponential increase in energy consumption coupled with rapid population growth, which has led to a dramatic increment in the emission of greenhouse gases (GHG), such as $CO_2$ [1]. The concentration of $CO_2$ in the atmosphere has increased by 40 % since the mid-nineteenth century, aggravating the effects of climate change [2]. Thus, the efforts have been focused on coming up a sustainable development model that guarantees a compromise between economic growth and the population's quality of life [3].

In this context, different strategies or technologies for minimizing this problem are being investigated. Power to gas (PtG) technology emerges as a promising technological alternative, since is considered an efficient way of storing renewable energy in form of so-called chemical energy carriers and, in particular, in form of methane ($CH_4$) or synthetic natural gas (SNG). The later process, known as power to methane technology (PtM), uses $CO_2$ as a raw material in a carbon neutral cycle, which contributes to the reduction of GHG. Specifically, it converts $CO_2$ into $CH_4$ by Sabatier catalytic reaction (Eq. (1)) [4], using renewable $H_2$, which is produced by water electrolysis [5]. Furthermore, this technological alternative allows the energy integration of the electricity network in the natural gas grid. In this way, fluctuations in the supply of renewable energies are mitigated, increasing the installed capacity and

* Corresponding author.
*E-mail address:* juanra.gonzalezvelasco@ehu.eus (J.R. González-Velasco).

https://doi.org/10.1016/j.jcou.2022.101888
Received 3 December 2021; Received in revised form 31 December 2021; Accepted 5 January 2022
Available online 13 January 2022

facilitating the decarbonisation of the electricity sector [6].

$$CO_2 + 4H_2 \rightleftarrows CH_4 + 2H_2O \quad \Delta_{298\,K} = -165\ kJ\ mol^{-1} \tag{1}$$

$CO_2$ methanation is a very exothermic reaction with a high equilibrium conversion within the temperature range from 25 °C to 400 °C and is favoured at low temperatures and high pressures [7]. In the presence of efficient catalysts, $CO_2$ methanation can be completed with a high value of selectivity towards $CH_4$ [8]. Transition metals, such as Ru, Rh, Pt, Pd, Ni and Co [9–15], are usually used as active phases. Among them, nickel is widely implemented due to its low cost, good activity and selectivity towards $CH_4$. These metals are usually supported on high surface area materials, such as $Al_2O_3$, $CeO_2$, $SiO_2$, $ZrO_2$, $TiO_2$ and zeolites [16–19]. The low price and additional promoter characteristics of $Al_2O_3$ and $CeO_2$ respectively, motivate their widespread implementation as $CO_2$ methanation supports. Thus, Ni/$Al_2O_3$ and Ni/$CeO_2$ formulations are the most commercialised catalyst at industrial level.

Although many formulations have been extensively characterized and catalytically tested, there is still controversy with regard to reaction mechanism and corresponding rate determining step (RDS). The first investigation about the kinetics of the methanation reaction was published in 1955 with pelletized Ni-Kieselguhr catalyst [20]. However, the proposed models at that time were limited to conditions of initial reaction rates, leading to preliminary kinetic models. Following studies were based on simple power-law mechanisms [21–23]. The first detailed mechanistic model was proposed 30 years later by Weatherbee et al. [24] for a 3% Ni/$SiO_2$ catalyst operating under differential reactions conditions at highly diluted gas streams. In their study, they assumed the dissociative adsorption of $H_2$ and $CO_2$ in form of [H], [CO] and [O]. The adsorbed [CO] dissociates again to [C] and [O]. Then, in later stages, the carbon is hydrogenated to [CH] as reaction intermediate in the methane formation, whereas the oxygen is hydrogenated to hydroxyl groups [OH] and, finally, to water. Kai et al. [25] achieved further progress on kinetic study with 17 wt.% Ni-$La_2O_3$/$Al_2O_3$ catalyst under differential and integral reaction conditions. In their study, kinetics was described in terms of Langmuir-Hinshelwood-HougenWatson (LHHW) mechanistic equation, based on that proposed by Weatherbee et al. [24], but assuming the hydrogenation of carbon as the rate limiting step, instead of CO dissociation.

These studies were followed by others based on different catalyst formulations or reactions mechanisms. In general, two widely accepted mechanisms have been proposed, based on IR characterization techniques: the so-called dissociative and associative mechanisms [26,27]. The former assumes the dissociative adsorption of $CO_2$ into adsorbed CO or carbonyl, followed by its hydrogenation into $CH_4$ [28,29], as previously proposed by Weatherbee et al. [24]. In the latter, by contrast, $CO_2$ is molecularly adsorbed in form of carbonates or bicarbonates, which are progressively reduced by $H^+$ spillover into formate, formyl, methoxy species and, finally, methane [30–32]. So, knowledge of adsorbed species that are formed during $CO_2$ methanation on catalyst surface by operando FTIR or in situ DRIFTS could be of great help when proposing kinetic models for precise fitting to experimental kinetic data and determining the RDS on a specific catalyst.

Only few works in recent literature have focused on the kinetics of $CO_2$ methanation on Ni-based [16,33–35] and Ru-based [36–38] catalysts. Among them, commercial or co-precipitated Ni/$Al_2O_3$-type formulation with high metal content (> 15 % of Ni) has been the most studied, since it is in turn the most used in industry for methanation processes [39–43]. Table S1 gives an overview of published models. However, to the best of the author's knowledge, not only the type of support and the presence of a secondary metal or promoter could alter the intrinsic kinetics of a catalyst (rate equations), but also the active metal content. Therefore, the main goal of this work is to determine a kinetic model to predict kinetics of $CO_2$ methanation on a Ni/$Al_2O_3$ catalyst with low metal content, which has recently been published [44], at industrially relevant conditions. For that, different kinetic models have been evaluated based on those reported in the literature and our previous operando FTIR and isotopic mechanistic studies [44,45].

In order to achieve this target, the basic physico-chemical properties of the catalyst are summarized as well as adsorbed species analyzed by in-situ DRIFTS. Then, the activity of the catalyst was evaluated at different temperatures, once steady state was reached. Finally, kinetic experiments were carried out both under differential and integral reactor conditions. For that, various power-law or Langmuir-Hinshelwood-Hougen-Watson (LHHW) type models were evaluated, considering our previous mechanistic studies and based on the more common reaction mechanisms previously reported. Knowledge of the reaction kinetics is critical for modeling, designing and optimization of $CO_2$ methanation industrial reactor.

## 2. Experimental

### 2.1. Catalyst preparation

The catalyst studied in this work (Ni/$Al_2O_3$) was prepared by the incipient wetness impregnation method as reported elsewhere [44]. For that, a commercial γ-$Al_2O_3$ supplied by *Alfa Aesar* (Stock Nº 43855) and $Ni(NO_3)_2{\cdot}6H_2O$ (*Sigma-Aldrich*) were used as support and nickel precursor, respectively. Firstly, a specific mass of nickel precursor was diluted in an ethanolic solution and impregnated over alumina support, the Ni content resulted in 9.5 wt.%. Finally, the catalyst was calcined at 600 °C in static air for 6 h using a heating rate of 5 °C $min^{-1}$.

### 2.2. Experimental setup

The catalytic tests were performed in a fixed-bed cylindrical reactor of 7 mm internal diameter. The catalyst, in powder form (0.3−0.5 mm), was mixed with quartz particles (0.5−0.8 mm) up to a total volume of 1 $cm^3$. Prior to the activity tests, the catalyst was pre-treated at 500 °C for 1 h under 20 % $H_2/N_2$ (250 $cm^3$ $min^{-1}$) mixture, and then cooled in pure $N_2$ to 200 °C. The feed composition during the activity test was 16 % of $CO_2$, 64 % of $H_2$ and 20 % of $N_2$, which corresponds to a $H_2$:$CO_2$:$N_2$ molar ratio of 4:1:1.25. The total flow rate was set at 250 $cm^3$ $min^{-1}$, equivalent to a space time ($W/F^0_{CO_2}$) of 4.67 g h $mol^{-1}$ and to a gas hour space velocity (GHSV) of 15,000 $h^{-1}$. The activity test (light-off curves) was carried out in the temperature range 200−500 °C in steps of 25 °C, with a heating rate of 5 °C $min^{-1}$ between steps. The outlet gas composition was measured on line, at each step under steady state conditions, with a gas chromatograph (Agilent HP7890B).

Once the light-off curve was obtained, the stability test was carried out with the same feed composition than in the standard activity test. Based on the evolution of the light-off curve with temperature, the reactor was kept at 400 °C for 72 h, measuring the outlet gas composition every 12 min.

The catalytic activity and stability were evaluated in terms of $CO_2$ conversion ($X_{CO_2}$) and selectivity towards $CH_4$ ($S_{CH_4}$) and CO ($S_{CO}$). In order to estimate these parameters the following expressions were used:

$$X_{CO_2} = \frac{F^{in}_{CO_2} - F^{out}_{CO_2}}{F^{in}_{CO_2}} \times 100 \tag{2}$$

$$S_{CH_4}(\%) = \frac{F^{out}_{CH_4}}{F^{out}_{CH_4} + F^{out}_{CO}} \times 100 \tag{3}$$

$$S_{CO}(\%) = \frac{F^{out}_{CO}}{F^{out}_{CH_4} + F^{out}_{CO}} \times 100 \tag{4}$$

$$Y_{CH_4}(\%) = \frac{F^{out}_{CH_4}}{F^{in}_{CO_2}} \times 100 \tag{5}$$

### 2.3. Design of kinetic experiments

In order to assure catalytic stability during whole process, a stability test was carried out at 400 °C and atmospheric pressure. Once the catalyst was stabilized, the kinetic study was performed. During the kinetics tests, operational parameters were varied in the following ranges: temperature, 315−430 °C; total flowrate, 200-1100 $cm^3\ min^{-1}$ (equivalent to GSHV of 12000−66000 $h^{-1}$ or $W/F^0_{CO_2}$ of 1.6–24.9 g h $mol^{-1}$); $H_2$ to $CO_2$ ratio ($H/C$) in the feedstream, 2–10; total pressure ($P$), 2−6 bar. These reaction conditions allowed us to study the effect of temperature, contact time and partial pressure of reagents/products on reaction rate. The reaction rates, obtained in the absence of mass transfers limitations, were used to estimate kinetic parameters under differential ($X_A < 10$ %) as well as integral ($X_A > 10$ %) reaction conditions; 0.5 g of $Ni/Al_2O_3$ catalyst was used for kinetic experiments under differential reactor conditions, whereas a sample mass of 1.0 g was used for the experiments under integral reactor conditions. Operational conditions along with corresponding activity parameters of all kinetic measurements are summarized in the Table A4 of the Appendix A4. In all experiments, $N_2$ was used as diluent to minimize heat and mass transfer effect.

### 2.4. In situ DRIFTS experiments

The $CO_2$ methanation reaction was monitored by in situ DRIFT spectroscopy using a Jasco infrared spectrometer, model FT/IR 4100, and a reaction cell for temperature and reaction gas control where the gas flows through the catalytic bed. 70 mg of undiluted $Ni/Al_2O_3$ catalyst was used. A reduction pretreatment was carried out in situ in 50 % $H_2$/He at 450 °C for 60 min, and then the reaction cell was cooled down to room temperature under $H_2$/He flow. A background spectrum was recorded in He at room temperature, and then, the methanation mixture with 16 % $CO_2$ + 64 % $H_2$ + He balance was fed to the reactor at 1 bar and 100 mL/min. The temperature was raised in steps of 50 °C up to 450 °C, and spectra were recorded after 60 min in isothermal conditions at each temperature with 1 $cm^{-1}$ resolution.

## 3. Methodology

### 3.1. Kinetic rate equations

Determining a kinetic model or rate equation consists basically of calculating the kinetic constants and reaction orders. These parameters can be calculated by different computational methods, including linear and non-linear regression. Nevertheless, in order to carry out the fit is necessary to dispose reaction rate data, which in turn, can be determined under differential ($X_A < 10$ %) or integral reactor conditions ($X_A > 10$ %).

Under differential reactor conditions, partial pressures of reagents scarcely change in the small reactor which behaves with the perfect mix hypothesis. Thus, the reaction rate of $CO_2$ disappearance can be considered the same in all positions of the catalyst bed, simplifying the calculation of $CO_2$ disappearance rate (average) to the following algebraic equation:

$$\overline{-r_{CO_2}} = F^0_{CO_2}\frac{X_{CO_2}}{W} \tag{6}$$

where, $F^0_{CO_2}$ is the molar $CO_2$ flow at reactor inlet (mol $h^{-1}$), $X_{CO_2}$ is the $CO_2$ conversion and $W$ is the catalyst weight (g).

In contrast, under integral reactor conditions ($X_A > 10$ %), the reaction rate value changes with the catalytic bed length, and the local longitudinal $-r_{CO_2}$ is estimated by numerical integration of the plug flow reactor design equation:

$$\frac{W}{F^0_{CO_2}} = \int_0^{X^{out}_{CO_2}} \frac{dX_{CO_2}}{-r_{CO_2}} = \int_0^{X^{out}_{CO_2}} \frac{dX_{CO_2}}{f(T, X_{CO_2})} \tag{7}$$

The regressed parameters basically consisted of kinetic ($k$) and adsorption equilibrium constants ($K_{H_2}$, $K_{CO_2}$, $K_{OH}$ and $K_{CO}$), which were calculated by Arrhenius law and Van't Hoff expression, respectively. Both types of equations were parameterized to minimize the correlation among preexponential factor ($A_0$) and activation energy ($E_A$) or adsorption enthalpies ($\Delta H$) resulting in the following expressions derived from Arrhenius equation:

$$k = k_0 \exp\left[-\frac{E_A}{R}\left(\frac{1}{T}-\frac{1}{T_{ref}}\right)\right] \tag{8}$$

and Van't Hoff equation:

$$K_i = K_{i0}\exp\left[-\frac{\Delta H}{R}\left(\frac{1}{T}-\frac{1}{T_{ref}}\right)\right] \tag{9}$$

where, $k$ and $K_i$ are kinetic and adsorption constants at different temperatures, whereas $k_0$ and $K_{i0}$ are reference constants at $T_{ref}$ (430 °C in this work).

Lastly, the equilibrium constant of $CO_2$ methanation ($K_{eq1}$) can be estimated at every temperature by the following empirical expression:

$$K_{eq1} = 137 \cdot T^{3.998}\exp\left(\frac{158.7}{RT}\right) \tag{10}$$

where R is the ideal gas constant, 8.314 J $K^{-1}$ $mol^{-1}$.

### 3.2. Computational methods

For the parameters estimation, the fit of experimental data was carried out by least squares method (nonlinear regression), which consist on finding minimum value of objective function:

$$SSE = \sigma^2 = \sum_i^N \left(y^{exp} - y^{calc}\right)^2 \tag{11}$$

This function describes the sum of squared residuals obtained from the difference among experimental and calculated variable $y$ (hereunder, reaction rate or conversion) for every point, being $N$ the total number of kinetic experiments. The fit together with estimation of some kinetic parameters was carried out by *lsqcurvefit* and *fminsearch* commands of MATLAB software (R2014b version). The former is a nonlinear least-squares solver, whereas the latter performs a non-linear multidimensional minimization without restrictions by the Nelder-Mead algorithm. For the *fminsearch* command the following optimization options were set: a function tolerance (TolFun) of $10^{-10}$, lower bound of step size (TolX) of $10^{-3}$ and a maximum of 500 interactions (iter).

On the other hand, the quality of the fit was estimated to carry out model discrimination by calculating absolute mean deviations as follows:

$$D(\%) = \sqrt{\frac{\sigma^2}{N}}\frac{1}{\bar{y}} \times 100 \tag{12}$$

where $\bar{y}$ is the mean value of experimental variable.

Regarding the numerical integrations of Eq. (7), they were accomplished by *ode23* command, which is able to solve nonstiff differential equation systems by adaptative Runge-Kutta algorithm of 2nd and 3rd order.

## 4. Results

### 4.1. Catalyst characterization

$Ni/Al_2O_3$ catalyst was prepared and widely characterized in our

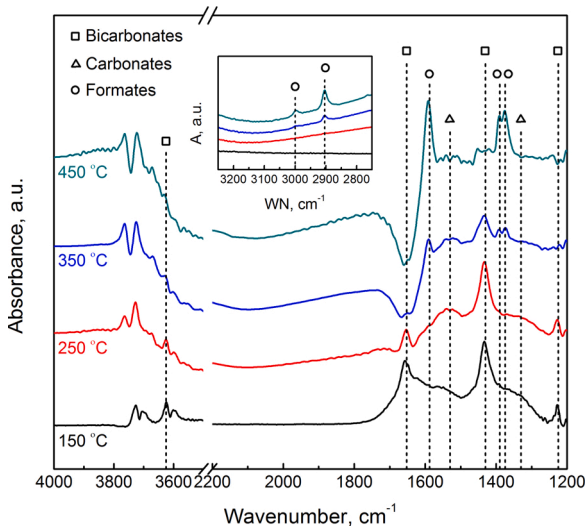


**Fig. 1.** In situ DRIFTS spectra recorded under 16 % $CO_2$/64 % $H_2$/He reaction stream at 150, 250 350 and 450 °C for 9.5 % Ni/$Al_2O_3$ catalyst.

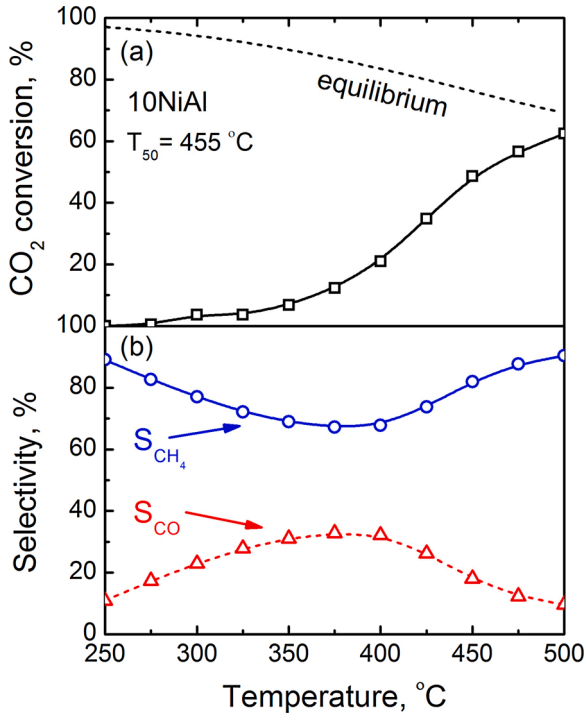


**Fig. 2.** (a) Light-off curve and (b) selectivity towards $CH_4$ ($S_{CH_4}$) and CO ($S_{CO}$) of Ni/$Al_2O_3$ catalyst recorded prior to the stability test. Reaction conditions: $P$ = 1 bar, $H_2/CO_2$ = 4 and $W/F_{A0}$= 4.7 g h $mol^{-1}$.

previous work [44]. Briefly, the Ni content was of 9.4 wt.% and its specific surface area of 172 $m^2$ $g^{-1}$, high enough to ensure a proper reagent-active sites contact. However, the reducibility or reduction degree of Ni at 500 °C was found to be low (9%), due to a high NiO-$Al_2O_3$ interaction or even $NiAl_2O_4$ formation (see Fig. S1). Although this indicates that much nickel will not be active during reaction (i.e., in the reduced state), the observed strong metal-support interaction suggest that its activity should be quite stable during the kinetic experiments. Hence, physico-chemical properties of 9.5 wt.% Ni/$Al_2O_3$ catalyst were considered adequate to achieve the kinetic study.

In order to determine the adsorbed species that could participate in reaction and get a first insight of the reaction pathway, in-situ DRIFTS during $CO_2$ methanation were carried out on 9.5 wt.% Ni/$Al_2O_3$ catalyst [44]. DRIFTS spectra recorded under $CO_2$ methanation conditions at different temperatures are shown in Fig. 1. Note that all spectra were recorded after 60 min exposure time, when the steady state conditions were reached.

The intense double band at 2350 $cm^{-1}$ (not shown) together with two double bands located at 3750−3500 $cm^{-1}$ confirm the presence of $CO_2$ gas in the cell. On the other hand, the bands appearing between 1800 and 1200 $cm^{-1}$ indicate the formation of adsorbed C-species on the catalyst surface during reaction, whose relative concentration changes with temperature. At 150 °C, 3 bands are clearly distinguishable at 1652, 1430 and 1225 $cm^{-1}$ which can be attributed to O—C—O stretching ($\nu_{OCO}$, both symmetric and asymmetric) and OH deformation ($\delta_{OH}$) of bicarbonate species. Moreover, the band corresponding to OH stretching vibration mode of bicarbonates is observed at 3625 $cm^{-1}$. As reported by other authors [30,31,38], the bicarbonates arise from $CO_2$ adsorption on OH– groups of γ-$Al_2O_3$. Additionally, other weak and broad bands can be observed at 1530 and 1330 $cm^{-1}$, which might be assigned to $\nu_{OCO}$ vibration modes of carbonate species in bidentate coordination. These carbonates could form from $CO_2$ adsorption on surface $O^{2-}$ (acting as Lewis basic sites) of both NiO and $Al_2O_3$ [44,46].

The increase of temperature leads to the depletion of bicarbonates/carbonates and the appearance of new bands at 1588 (asymmetric O—C—O stretching), 1390 (CH deformation) and 1375 $cm^{-1}$ (O—C—O stretching) which are characteristics of formate species adsorbed on $Al_2O_3$ [38]. Besides, the weak bands at around 3000 and 2900 $cm^{-1}$ ($\nu_{CH}$) confirm the presence of this species, which could be reaction intermediates [30,31]. The evolution of bands with temperature suggests that formates might come from nickel-assisted hydrogenation of bicarbonates or carbonates through $H^+$ spillover mechanism. Besides, note that the three bands of formates are clearly observed at 450 °C indicating that these species are quite stable with temperature. However, no characteristic bands of methane are observed to verify the participation of formate in the reaction.

The increase of the baseline slope below 2000 $cm^{-1}$ could be due to the formation of Ni-carbonyls, since these species yield broad bands in the 2200−1800 $cm^{-1}$ region with several contributions depending on the nature of the chemisorption site. The low intensity of the Ni-carbonyl broad signal suggests that their surface population is low, probably due to the low fraction of reduced nickel on this catalyst, and get masked by the behavior of other higher-intensity signals (mainly the bicarbonates band at 1652 $cm^{-1}$). Much more intense Ni-carbonyl signal was observed in our previous work by operando FTIR measurements [45] during $CO_2$ methanation over other Ni/$Al_2O_3$ catalysts with similar nickel contents. It was concluded in that case that the reaction proceeds via formation of carbonyl species, mainly arising from intermediate formates decomposition, followed by its hydrogenation into $CH_4$. Actually, as it will be concluded afterwards from the kinetic fitting, carbonyls seem to play a key role as reaction intermediates also with the Ni/$Al_2O_3$ catalyst used in the current study, despite the DRIFTS experiments suggest low surface population in comparison to other surface species.

As a summary, the DRIFTS results show several surface species that form and disappear during reaction, including carbonyls, formates, bicarbonates and carbonates, but is not possible to distinguish between spectators and reaction intermediates. This information will be used to propose different reaction mechanisms, which will be evaluated by a kinetic study over a wide range of operation conditions.

### 4.2. Catalyst activity and stability

Activity and stability tests were carried out to evaluate the efficiency of Ni/$Al_2O_3$ catalyst in $CO_2$ methanation reaction and to ensure its stability during kinetic experiments, respectively. Prior to the stability test, the activity of 9.5 wt.% Ni/$Al_2O_3$ catalyst was tested varying the temperature from 250 to 500 °C. Fig. 2a shows the light-off curve of the

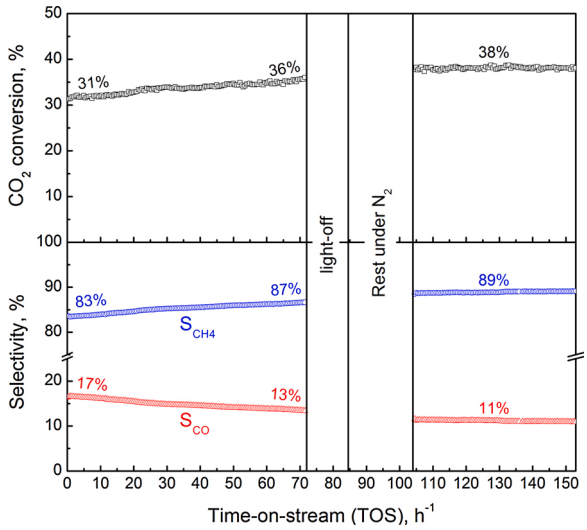


**Fig. 3.** (a) $CO_2$ conversion and (b) selectivity towards methane ($S_{CH_4}$) and carbon monoxide ($S_{CO}$) during stability test at 400 °C.

$Ni/Al_2O_3$ catalyst, whereas Fig. 2b displays its selectivity towards methane ($S_{CH_4}$) and carbon monoxide ($S_{CO}$) as a function of temperature.

The Ni-based catalyst shows poor activity, being its $X_{CO_2} = 21$ % at 400 °C and achieving a $CO_2$ conversion of 50 % at $T_{50} = 455$ °C. Besides, its selectivity to non-desirable CO ($S_{CO}$) is higher than 10 % in the entire temperature range, observing a maximum value of 33 % at 375 °C. The expected low activity and $CH_4$ selectivity of this catalyst is related to its high metal-support interaction. As previously described, the reducibility of this catalyst at 500 °C is less than 10 %. Taking into account that 500 °C is the temperature used during activation of the catalyst prior to activity test, only a small fraction of Ni has been activated during the one-hour reduction with 20 $\%H_2/N_2$, which results in a low $CO_2$ hydrogenation activity.

After that, the reaction temperature was kept at 400 °C during 72 h, with the same feed composition than in the activity test (250 ml $min^{-1}$ of 16 % $CO_2$/64 % $H_2/N_2$). The evolution of $CO_2$ conversion and selectivity with time-on-stream (*TOS*) is shown in Fig. 3. Note that by increasing *TOS* up to 72 h approximately, the $CO_2$ conversion slowly rises from 31 to 36 %. These results suggest that the catalyst is being activated during the stability test. This trend is because part of remaining NiO is reduced, leading to a higher active metal surface. Likewise, the selectivity towards $CH_4$ increases from 83 to 87 % since the catalyst has a major capacity to dissociate $H_2$ and convert $CO_2$ exclusively into $CH_4$ (Fig. 3b). Immediately after 72 h on stream, the sample was exposed again to temperature changes under reaction mixture (intermediate light-off), in order to accelerate the activation and stabilization of the catalyst by reduction of additional NiO sites. After that, $CO_2$ conversion at 400 °C only increased from 36 to 38 %. In fact, no relevant changes were observed in $X_{CO_2}$ (38 %) and $S_{CH_4}$ (89 %) during last 48h-on-stream, indicating that reduced Ni particles did not suffer from sintering or any other deactivation mechanism and, as a consequence, the activity of the catalyst had been stabilized.

### 4.3. Model and kinetic parameter estimation

Once the catalyst stabilized, the kinetic study was carried out under a wide variety of operational conditions (Table A4). In this study, rates of $CO_2$ hydrogenation both in differential ($X_A < 10$ %) and integral modes ($X_A > 10$ %) are calculated for further estimation of apparent reaction orders, activation energies, kinetic as well as adsorption constants, and choosing the kinetic model that best fits experimental data.

#### 4.3.1. Apparent reaction orders and activation energy estimation

In order to study the effect of reagents and products partial pressures on the $CO_2$ hydrogenation rate, the experimental data set obtained at 325 °C were employed. For all those kinetic experiments, the $CO_2$ conversion is lower than 10 %; and therefore, the $CO_2$ disappearance rate

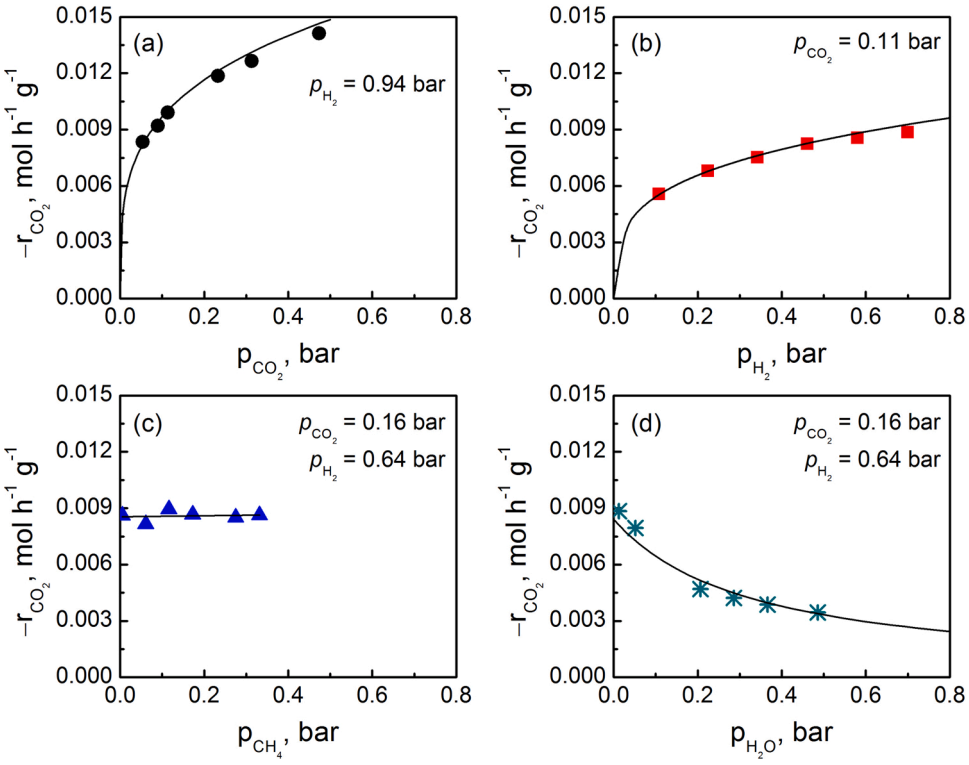


**Fig. 4.** Influence of: (a) $CO_2$ ($p_{CO_2}$), (b) $H_2$ ($p_{H_2}$), (c) $CH_4$ ($p_{CH_4}$) and (d) $H_2O$ ($p_{H_2O}$) partial pressures on $CO_2$ methanation rate at 325 °C. Total pressure of 2 bar and GHSV = 30,000 $h^{-1}$.

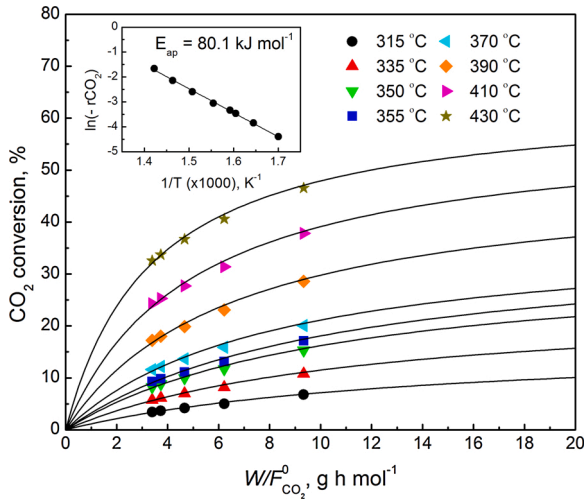


**Fig. 5.** Effect of space-time ($W/F^0_{CO_2}$) on $CO_2$ conversion at different temperatures together with Arrhenius plot. Symbols refer to experimental data and black lines to the obtained fits. Total pressure of 2 bar and $H_2/CO_2$ ratio in the feedstream of 4.

**Table 1**
Apparent activation energies of different formulations reported in the literature compared to the obtained in this work for 9.5 wt.% $Ni/Al_2O_3$ catalyst.

| Formulation | Ea (kJ $mol^{-1}$) | Reference |
|---|---|---|
| 10 wt.% $Ni/Al_2O_3$ | 89.0 | [54] |
| 10 wt.% $Ni/Al_2O_3$_ordered mesoporous | 75.2 | [48] |
| 20 wt.% $Ni/Al_2O_3$ | 83.0 | [55] |
| 16.7 wt.% Ni-x% $La/Al_2O_3$ | ≈80.0 | [49] |
| $NiAl(O)_x$ | 83.0 | [39] |
| $Ni/(Al_2O_3{\cdot}3Ca)$ | 118.7 | [41] |
| Ni/Al hydrotalcite-derived | 75.0 | [42] |
| $Ni/SiO_2$ | 79.0 | [33] |
| Ni/MgO | 99.0 | [34] |
| $Ni/CeO_2$ | 112.2 | [16] |
| 9.5 wt.% $Ni/Al_2O_3$ | 91.6 | This work |

can be calculated according to Eq. (6). Note that the partial pressures shown in this section refer to the average among the observed at differential reactor inlet and outlet, in fact, $CO_2$ methanation rate is also calculated as an average inside the reactor.

Fig. 4 shows $CO_2$ disappearance rate as a function of reagent and products concentration at 325 °C. It can be clearly observed that reaction rate increases with $CO_2$ partial pressure ($p_{CO_2}$) following saturation trend (Fig. 4a). In fact, by increasing $p_{CO_2}$ from 0.05 to 0.23 bar and then, from 0.23 to 0.47 bar, $-r_{CO_2}$ rises by 42 and 19 %, respectively. This trend is in agreement with results reported by Weatherbee et al. in 1982 [24], according to which the $CO_2$ hydrogenation is quite sensitive to $CO_2$ concentration at low partial pressures. On the other hand, Fig. 4b also shows a positive effect of $H_2$ partial pressure ($p_{H_2}$) on $-r_{CO_2}$. Specifically, $-r_{CO_2}$ increases around 59 % varying the $H_2$ partial pressure from 0.11 to 0.70 bar.

The influence of reagents was further analyzed fitting the data to a simple power-law expression of the form:

$$-r_{CO_2} = k p^{\alpha}_{CO_2} p^{\beta}_{H_2} \tag{13}$$

where $k$ is the kinetic constant at 325 °C; $\alpha$ ($CO_2$) and $\beta$ ($H_2$) are the apparent reaction orders. By logarithmic linearization and multiple linear regression, the apparent reaction orders of $CO_2$ and $H_2$ at 325 °C were estimated, resulting in 0.24 and 0.27, respectively. Namely, both reagents have similar influence on the $CO_2$ reaction rate. Noteworthy, Lefebvre et al. [33] also reported same order values of $CO_2$ and $H_2$ apparent orders at 300 °C for $Ni/SiO_2$ catalyst (0.30 and 0.42, respectively).

The influence of $CH_4$ ($p_{CH_4}$) and $H_2O$ ($p_{H_2O}$) partial pressures is shown in Fig. 4c and d, respectively. In both cases, $CO_2$ and $H_2$ partial pressures were kept at 0.16 and 0.64 bar, respectively. As reported by many authors [33,39,47], $-r_{CO_2}$ is almost insensitive to methane partial pressure, which denotes a reaction order close to 0. However, varying $H_2O$ partial pressure from 0 to 0.49 bar a considerable decrease in $-r_{CO_2}$ is observed, indicating that water strongly adsorbs on active sites hindering the reagents adsorption and hence, inhibiting the $CO_2$ hydrogenation rate. This is suggesting that the kinetic constant depends on the concentration of adsorbed water or hydroxyls (OH–). Then, Eq. (13) could hardly predict the observed water resistance to reaction rate (Fig. 4d) and it must be modified as follows [42]:

$$-r_{CO_2} = \frac{k p^{\alpha}_{CO_2} p^{\beta}_{H_2}}{1 + K_{H_2O} p_{H_2O}} \tag{14}$$

where, $K_{H_2O}$ is the water adsorption constant at 325 °C.

Eq. (14) was linearized representing $1/-r_{CO_2}$ vs. $p_{H_2O}$ and fitted to experimental data. From the intercept and slope of the regression line, the kinetic and water adsorption constants were estimated resulting in 0.0157 mol $h^{-1}$ $g^{-1}$ $bar^{-0.57}$ and 3.061 $bar^{-1}$, respectively. Note that these values are reliable since they are positive and of the order of those reported in literature [43].

Once the effect of reactant and products concentration was studied, the apparent activation energy was determined in the 315–430 °C temperature region. Fig. 5 plots $CO_2$ conversion as a function of temperature and space time $\left(W/F^0_{CO_2}\right)$. As shown in the figure (black lines), experimental points were fit to a mathematical expression which considers thermodynamic equilibrium:

$$-r_{CO_2} = \frac{\left(W/F^0_{CO_2}\right)^b}{a + \left(W/F^0_{CO_2}\right)^b / X_{eq}} \tag{15}$$

where, $a$ and $b$ are the fitting coefficients and $X_{eq}$ is the equilibrium conversion depending on temperature.

It can be observed that $X_{CO_2}$ tends towards saturation (at $T > 335$ °C), as is usual under integral reactor conditions. Therefore, the initial reaction rates approach was chosen in this case to calculate apparent kinetic constants. This method consists of fitting conversion vs. space-time curves, which extrapolation at $W/F^0_{CO_2} = 0$ and corresponding derivatives results in values of initial reaction rates at every temperature,

$$-r^0_{CO_2} = \left(\frac{dX_{CO_2}}{d(W/F^0_{CO_2})}\right)_{W/F^0_{CO_2}=0} = k_{ap}\, f(C^0_{CO_2}, C^0_{H_2}) \tag{16}$$

that together with logarithmic Arrhenius expression:

$$\ln\left(-r^0_{CO_2}\right) = \ln\left[A_0 f(C^0_{CO_2}, C^0_{H_2})\right] - \frac{E_{ap}}{R}\left(\frac{1}{T}\right) \tag{17}$$

allows determination of the apparent activation energy from the slope of linear plot of $\ln\left(-r^0_{CO_2}\right)$ vs. $1/T$, as represented in the inset plot of Fig. 5.

The apparent activation energy for $CO_2$ hydrogenation (to CO as well as $CH_4$) on 9.5 wt.% $Ni/Al_2O_3$ catalyst resulted 80.1 kJ $mol^{-1}$. The determination of activation energy values has already been conducted by other authors (Table 1), observing similar values that range from 75.0 to 118.7 kJ $mol^{-1}$ on NiAl-type catalysts [33,39,41,42,48,49].

Finally, the reliability of calculated apparent activation energies was checked by Mears [50] and Anderson [51] criteria. Despite the high reaction heat of $CO_2$ methanation ($\Delta H = -165$ kJ $mol^{-1}$), it should be noted that both criteria were satisfied indicating that the activation energies were correctly deduced from the Arrhenius expression. As shown in Table S2, dimensionless values are below 0.15 and 0.75,

**Table 2**
Elementary steps of conventional dissociative CO formation mechanism.

| Step | Reaction | Assumption |
|---|---|---|
| 1 | $H_2 + 2^* \rightleftarrows 2H^*$ | Quasi equilibrium |
| 2 | $CO_2 + 2^* \rightleftarrows CO^* + O^*$ | Quasi-equilibrium |
| 3 | $CO^* \rightleftarrows CO(g) + *$ | Quasi-equilibrium |
| 4 | $CO^* + H^* \rightleftarrows CHO^* + *$ | Rate determining step |
| 5 | $CHO^* + * \rightleftarrows CH^* + O^*$ | Low CHO* coverage |
| 6 | $CH^* + 3H^* \rightleftarrows CH_4^* + 3^*$ | Low $CH_x$* coverage |
| 7 | $CH_4^* \rightleftarrows CH_4(g) + *$ | Low $CH_4$* coverage |
| 8 | $O^* + H^* \rightleftarrows OH^* + *$ | Low O* coverage |
| 9 | $OH^* + H^* \rightleftarrows H_2O^* + *$ | Quasi-equilibrium |
| 10 | $H_2O^* \rightleftarrows H_2O(g) + *$ | Low $H_2O$* coverage |

**Table 3**
Elementary steps of proposed H-assisted CO formation mechanism.

| Step | Reaction | Assumption |
|---|---|---|
| 1 | $H_2 + 2^* \rightleftarrows 2H^*$ | Quasi equilibrium |
| 2 | $CO_2 + OH^* \rightleftarrows HCO_3^*$ | Quasi-equilibrium |
| 3 | $HCO_3^* + H^* \rightleftarrows HCOO^* + OH^*$ | Quasi-equilibrium |
| 4 | $HCOO^* + * \rightleftarrows CO^* + OH^*$ | Rate determining step |
| 5 | $CO^* \rightleftarrows CO(g) + *$ | Quasi-equilibrium |
| 6 | $CO^* + H^* \rightleftarrows CHO^* + *$ | Low CO* coverage |
| 7 | $CHO^* + * \rightleftarrows CH^* + O^*$ | Low CHO* coverage |
| 8 | $CH^* + 3H^* \rightleftarrows CH_4^* + 3^*$ | Low $CH_x$* coverage |
| 9 | $CH_4^* \rightleftarrows CH_4(g) + *$ | Low $CH_4$* coverage |
| 10 | $O^* + H^* \rightleftarrows OH^* + *$ | Low O* coverage |
| 11 | $OH^* + H^* \rightleftarrows H_2O^* + *$ | Quasi-equilibrium |
| 12 | $H_2O^* \rightleftarrows H_2O(g) + *$ | Low $H_2O$* coverage |

indicating that thermal gradients can be considered apparently negligible both in the film around the catalyst as well as inside the catalyst particle.

#### 4.3.2. LHHW-type kinetic equations

LHHW-type equations, which are based on reaction mechanism and attempt to predict the rate of the slowest step of the reaction pathway, are applicable in a wider range than power-law equations. The first step in the design of LHHW equation is the proposal of a reaction mechanism. It has been already mentioned that $CO_2$ methanation can proceed via associative or dissociative type mechanisms, depending if $CO_2$ molecule is either directly hydrogenated or previously split, respectively. The kinetic results reported in Table A4 reveal the appearance of considerable amounts of CO, especially at low space times, since a higher difference between $CO_2$ conversion and $CH_4$ yield can be observed under these conditions. This trend suggests that adsorbed CO or carbonyls are formed during $CO_2$ hydrogenation on $Ni/Al_2O_3$ catalyst. According to previously reported mechanism [45], carbonyls can act as intermediates and operando FTIR experiments carried out over other $Ni/Al_2O_3$ catalyst suggested that $CO_2$ methanation proceeds via formation of carbonyl species mainly arising from intermediate formates decomposition, followed by its hydrogenation into $CH_4$.

Trying to clarify what the real reaction mechanism is, two reaction pathways are proposed in Tables 2 and 3, classified as dissociative or H-assisted mechanism depending on how CO is formed. Note that from each mechanism at least 10 equations can be derived assuming that one step among adsorption, reaction or desorption steps is the rate determining step (RDS). Models were derived from most probable RDS steps and for simplicity, just two LHHW-type equations with the best fit are shown in this section.

The first mechanism follows reaction pathway summarized in Table 2 and assumes that $H_2$ and $CO_2$ are dissociatively adsorbed forming hydrogen atoms (H) and carbonyls (CO) on Ni° surface [29]. Then, carbonyls react with dissociated hydrogen into carbon-hydroxy or adsorbed formyl (CHO, step 4). Subsequently, there is another carbon-oxygen cleavage yielding carbenes ($CH_x$, step 6), which are further hydrogenated into methane (step 7). At the same time, adsorbed oxygen atoms are sequentially hydrogenated into hydroxyls and water (steps 8 and 9). Note that under certain conditions carbonyls can be desorbed as $CO_{gas}$ instead of being hydrogenated (step 3). As the hydrogenation of carbonyl has been reported to be quite slow [39–42], step 4 was considered the RDS. The previous steps as well as step 9 are assumed to be at quasi-equilibrium, whereas the rest of steps are kinetically irrelevant due to the low coverage of reaction intermediates (extremely fast steps) [40,47]. Considering those premises, the following rate equation of $CO_2$ methanation is derived, which deduction is included in Appendix A2:

$$-r_{CO_2} = \frac{k_4 p_{CO_2}^{0.5} p_{H_2}^{0.5} \left(1 - \frac{p_{CH_4} p_{H_2O}^2}{p_{CO_2} p_{H_2}^4 K_{Eq1}}\right)}{\left(1 + \sqrt{K_{H_2} p_{H_2}} + \sqrt{K_{CO_2} p_{CO_2}} + K_{OH} \frac{p_{H_2O}}{p_{H_2}^{0.5}}\right)^2} \quad (18)$$

where $k_4$ is the kinetic constant and $K_{H_2}$, $K_{CO_2}$ and $K_{OH}$ are the $H_2$, $CO_2$ and hydroxyl adsorption constants. The kinetic constants are calculated by Arrhenius law (Eq. (8)), whereas the adsorption ones by Van't Hoff expression (Eq. (9)) and the equilibrium constant of $CO_2$ methanation ($K_{eq1}$) by Eq. (10). Finally, the reagents and products partial pressures are estimated according to Eqs. (A4.1)–(A4.5) of Appendix A4.

In the second mechanism (Table 3), $H_2$ also dissociates on $Ni^0$ surface into adsorbed H-atoms, whereas $CO_2$ is molecularly chemisorbed on surface OH– groups of $Al_2O_3$ forming bicarbonates ($HCO_3$). After that, bicarbonates close to metal particles react with dissociated $H_2$ by H spillover mechanism yielding formate species (HCOO) [38], which are decomposed into hydroxyls and carbonyls adsorbed on alumina and Ni surface (step 4). Subsequently, carbonyls are desorbed as carbon monoxide (step 5) and/or sequentially reduced up to $CH_4$ via $CH_xO$ intermediate species (steps 6–9). As in the first proposed mechanism, surface oxygen atoms as well as hydroxyls are hydrogenated into water (second product) in lumped steps.

In this case, step 4 was also chosen as the rate determining step since DRIFTS results revealed (Fig. 1) that formates could be intermediate species of $CO_2$ methanation. In fact, such species usually appear at high surface concentration in many FTIR or DRIFTS measurements [28,30,31,38] and have been considered in formulating various kinetic models [16,47]. On the other hand, adsorbed $H_2$, formate, hydroxyls and carbonyls are assumed to be in high enough concentration, partially covering the active sites and inhibiting $CH_4$ formation rate.

Thus, the second rate equation, which deduction is included in Appendix A3 (Eq. (A3.15)), is as follows:

$$-r_{CO_2} = \frac{k_4 p_{CO_2} p_{H_2}^{0.5} \left(1 - \frac{p_{CO} p_{H_2O}}{p_{CO_2} p_{H_2} K_{eq2}}\right)}{\left(1 + \sqrt{K_{H_2} p_{H_2}} + K_{CO_2} p_{CO_2} \sqrt{K_{H_2} p_{H_2}} + K_{OH} \frac{p_{H_2O}}{p_{H_2}^{0.5}} + K_{CO} p_{CO}\right)^2} \quad (19)$$

where $K_{eq2}$ is the equilibrium constant of reverse water gas shift reaction ($K_{RWGS}$), which can be deduced at every reaction temperature from water gas shift (WGS) equilibrium constant expression [52]:

$$\ln(K_{WGS}) = -3.732 + \frac{3850}{T} + \left(\frac{470}{T}\right)^2 \quad (20)$$

and, then, the reverse-WGS equilibrium constant is:

$$K_{RWGS} = \frac{1}{K_{WGS}} \quad (21)$$

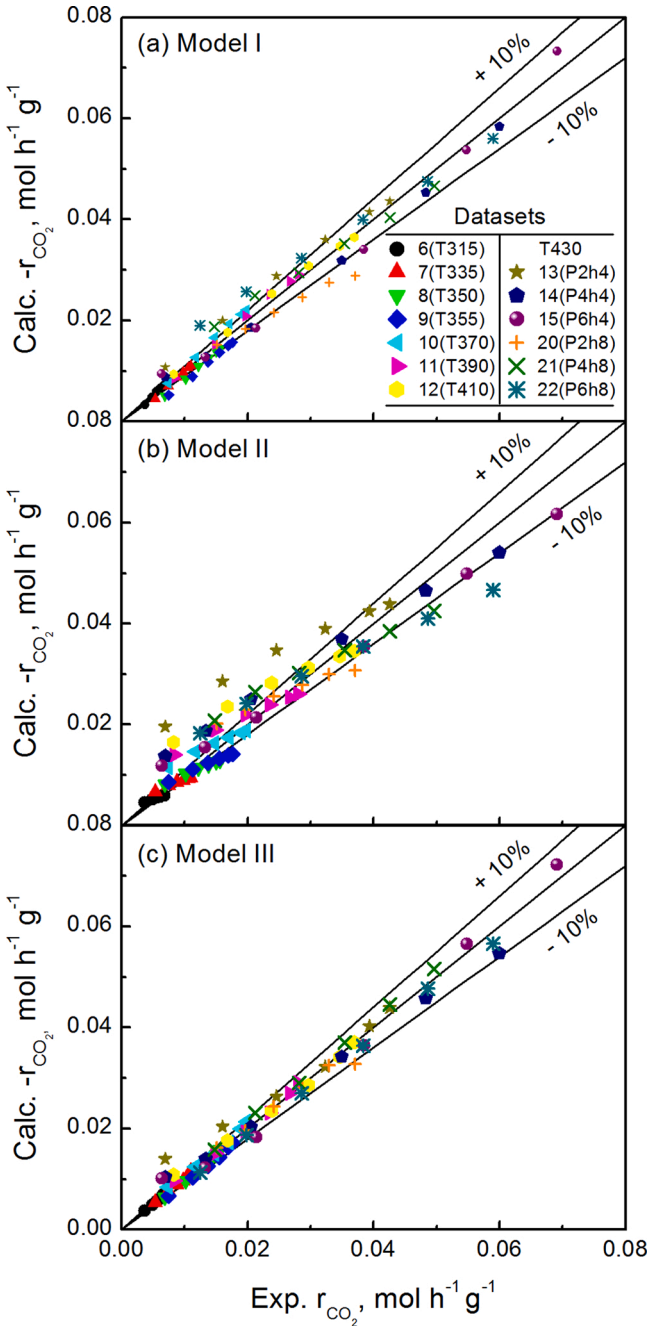


**Fig. 6.** Parity plots of: (a) power-law with $H_2O$ inhibition, (b) carbonyl dissociative and (c) H-assisted CO formation models adjusted to experimental data obtained operating with differential reaction conditions, i.e. total pressure (P2, P4, P6 = 2, 4 or 6 bar) and $H_2$ to $CO_2$ ratio in the feedstream (H/C4 and H/C8 correspond to $H_2/CO_2$ of 4 and 8, respectively).

### 4.3.3. Model discrimination by differential method data analysis

Once various kinetic models were proposed, $CO_2$ hydrogenation rates were calculated at different temperatures and space-times either deriving graphically $X_{CO_2}$ vs. $(W/F^0_{CO_2})$ curves in Fig. 5 or from analytical derivative of Eq. (15):

$$-r_{CO_2} = \frac{a \cdot b \cdot \left(W \Big/ F^0_{CO_2}\right)^{(b-1)}}{\left(a + \left(W \Big/ F^0_{CO_2}\right)^{b} \Big/ X_{eq}\right)^2} \quad (22)$$

Then, the model discrimination was carried out based on variance

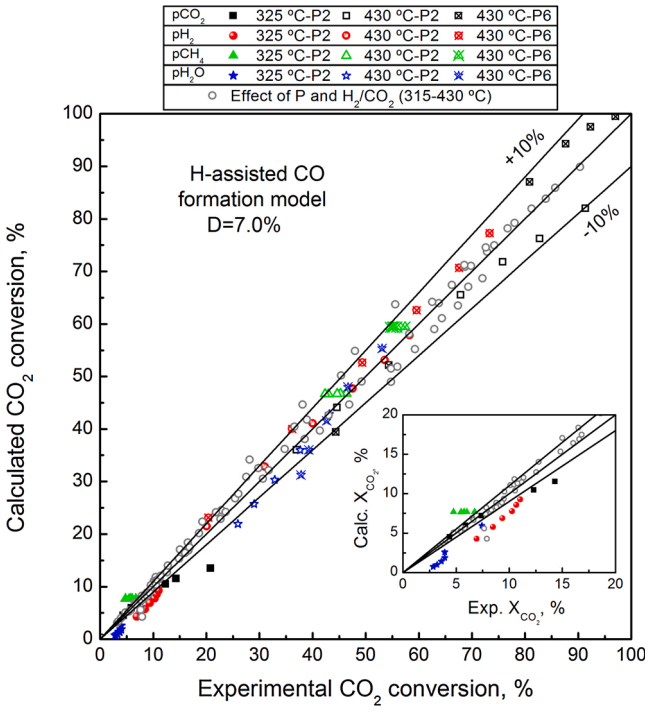


**Fig. 7.** Parity plot of H-assisted CO formation model adjusted to experimental data obtained operating with differential as well as integral reactor conditions. Black, red, green and blue symbols were obtained with different $CO_2$ ($p_{CO_2}$), $H_2$ ($p_{H_2}$), $CH_4$ ($p_{CH_4}$) and $H_2O$ ($p_{H_2O}$) partial pressures, respectively. Hollow black circles (○) correspond to data plotted in Fig. 6.

**Table 4**
Kinetic as well as adsorption constants estimated at different temperatures.

| | Kinetic constants | | Adsorption constants | | |
|---|---|---|---|---|---|
| $T$ (°C) | $k_4$ (mol (g h)$^{-1}$ atm$^{-1.5}$) | $k_6$ (mol (g h)$^{-1}$ atm$^{-1.5}$) | $K_{HCOO}$ (atm$^{-1.5}$)* | $K_{OH}$ (atm$^{-0.5}$) | $K_{CO}$ (atm$^{-1}$) |
| 315.15 | 0.105 | 6.66 | 0.430 | 5.20 | 166.0 |
| 325.15 | 0.143 | 7.29 | 0.418 | 4.76 | 143.2 |
| 335.15 | 0.194 | 7.95 | 0.407 | 4.37 | 124.2 |
| 350.15 | 0.299 | 9.01 | 0.392 | 3.86 | 101.1 |
| 355.15 | 0.345 | 9.38 | 0.388 | 3.71 | 94.6 |
| 370.15 | 0.519 | 10.55 | 0.374 | 3.30 | 78.0 |
| 390.15 | 0.870 | 12.23 | 0.358 | 2.85 | 61.1 |
| 410.15 | 1.415 | 14.06 | 0.343 | 2.49 | 48.6 |
| 430.15 | 2.239 | 16.04 | 0.330 | 2.18 | 39.2 |

* $K_{HCOO} = K_{CO_2}\sqrt{K_{H_2}}$ (Eq. (21)).

(Eq. (11)) as well as mean absolute deviation (Eq. (12)) values.

Fig. 6 shows the parity plots of power law and LHHW kinetic models. After regression, the power law model with water inhibition (Fig. 6a) presents a mean absolute residual of 11.5 %. Although the fit quality is acceptable, the model underestimates the $CO_2$ disappearance rate at low temperature (< 370 °C) and does not predict satisfactorily data at 430 °C, which includes the experiments where $CO_2$ methanation rate is boosted by increasing $H_2/CO_2$ molar ratio into 8 and total pressure is varied from 2 to 6 bar. Thus, although this model fits satisfactorily kinetic data on a commercial $Ni/SiO_2$ catalyst [33], it is not suitable to describe some mechanistic aspects observed during FTIR experiments in our case. Nevertheless, it must be highlighted that prediction was considerably improved by adding the water adsorption constant to Eq. (13). In fact, considering the water inhibition effect, the absolute mean deviation was decreased from 38.6 % ($\sigma^2 = 6.10{\cdot}10^{-3}$) to 11.5 % ($\sigma^2 = 4.93{\cdot}10^{-4}$).

The fitting quality of the carbonyl model (Fig. 6b), which is derived

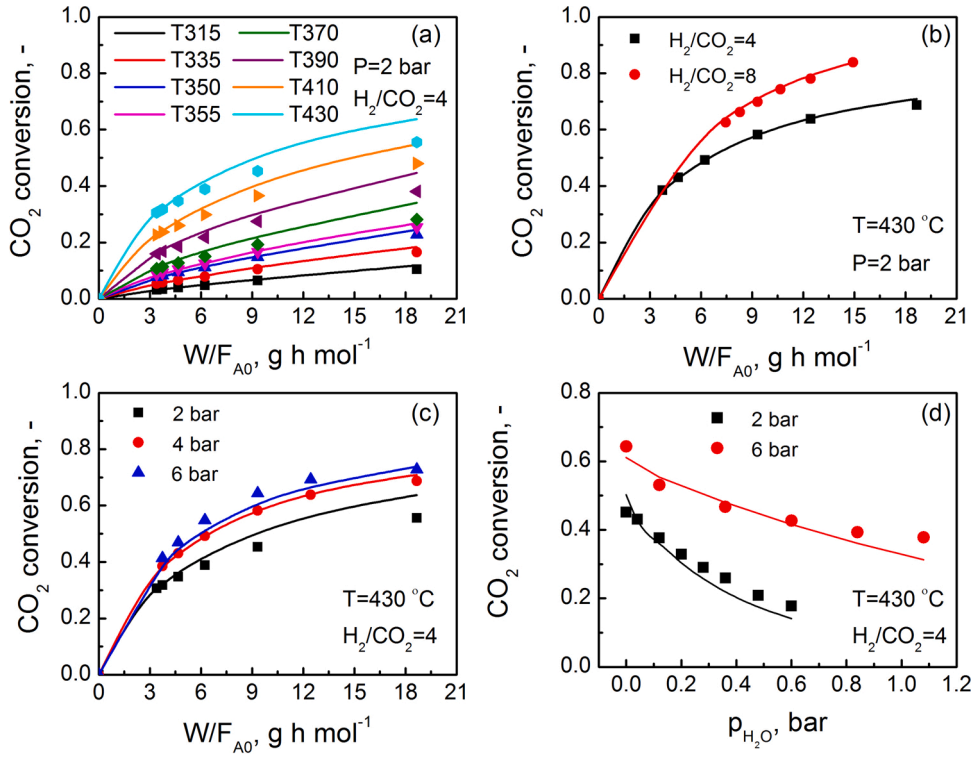


**Fig. 8.** Comparison of experimental (points) and predicted (lines) $CO_2$ conversion as a function of: (a) reaction temperature at increasing space times (2 bar), (b) $H_2$ to $CO_2$ ratios and, (c) $H_2$ and (d) $H_2O$ partial pressure at the inlet, for two different system pressures (2 and 6 bar) in the case of the later.

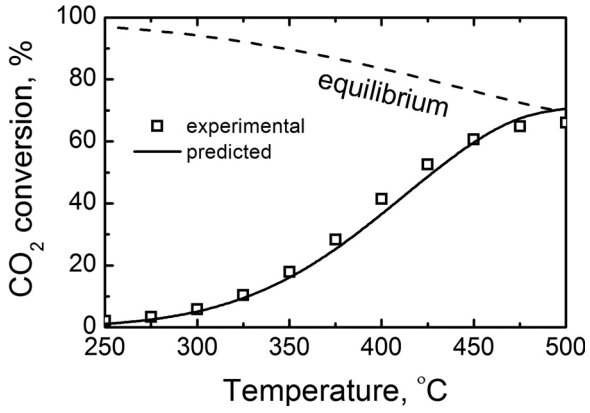


**Fig. 9.** Comparison of experimental light-off curve (points) and predicted one (line) for a feed composition of 16 % of $CO_2$, 64 % of $H_2$ and 20 % of $N_2$, and total pressure of 1 bar.

from dissociative CO formation mechanism and assumes the hydrogenation of carbonyl as RDS, proved to be less significant than that of potential model including water inhibition. In fact, only a few points were within ± 10 % dispersion region, being its mean absolute residual 20.1 % ($\sigma^2 = 1.50{\cdot}10^{-3}$). This LHHW model systematically underestimates $-r_{CO_2}$ under differential reactor conditions ($T < 355$ °C) and then overestimates it with increasing temperature, observing the highest deviations (even superior to 100 %) at 430 °C (P2-H/C4 dataset). Although this model has currently been validated by many authors who have studied kinetics on $Ni/Al_2O_3$ and $NiAl(O)_x$ formulations with high Ni content (> 15 wt%) [39–42], in our study it presents lower statistical significance than potential-law model and hence should be discarded. The worse fit could be related with differences in Ni loading, Ni reduced state and Ni particle size, parameters which alter the way that $CO_2$ is adsorbed onto the catalyst [53]. Unlike $Ni/Al_2O_3$ samples with high metal loading, 9.5 wt.% $Ni/Al_2O_3$ catalyst contains poor reducibility and metal surface area resulting in low affinity to CO adsorption (i.e., low carbonyl concentration), as evidenced by the lack of FTIR carbonyl bands (see Fig. 1). That may be the reason why the fitting quality of this model, which RDS is the hydrogenation of adsorbed CO, is statistically less significant than other studies reported in literature.

Finally, the H-assisted CO formation model, here proposed based on DRIFTS (Fig. 1) and previous operando FTIR results [45], shows the lowest variance ($\sigma^2 = 2.40{\cdot}10^{-4}$) and a mean absolute deviation of 8.0 % (Fig. 6c). Noteworthy, almost all points are within ± 10 % dispersion region and not systematic deviation is noticed, i.e., the kinetic equation is able to describe the effect of temperature, pressure as well as $H_2/CO_2$ molar ratio over the wide range of conditions employed. The obtained regression results, together with the fact that formates and CO gas are observed by DRIFTS, clearly suggest that carbonyls arise from formates following the associative mechanism rather than through $CO_2$ dissociative adsorption. In fact, here proposed model shows a significant decrease (12.1 %) in absolute mean residual compared to the previous potential model with $H_2O$ inhibition.

### *4.4. Extended model validation and parameter estimation by integral method data analysis*

In the last step, adsorption constants and enthalpies were estimated by integral method of data analysis (numerical integration of Eq. (7) together with nonlinear regression. In this case, all kinetic measurements were employed, including dataset in which partial pressures of one of the reagents and products is varied, with the aim of determining adsorption parameters with more certainty. However, the presence of considerable amount of CO at low space-times and high temperatures, could not be neglected when integrating design equation, since partial pressures included in the mechanistic equation are function of both methane ($Y_{CH_4}$) and CO ($Y_{CO}$) yields. Therefore, other rate equations must be incorporated to the system to carry out the integration properly, which describe the formation rate of $CH_4$ and CO. In this work, step 6 of

H-assisted CO formation mechanism, the hydrogenation of carbonyl into formyl, is the one that makes most sense to be the rate determining step of CO methanation. From such assumption the following equation, deduced in the Appendix A3 (Eq. (A3.19)), is derived:

$$r_{CH_4} = \frac{k_6 p_{CO} p_{H_2}^{0.5}\left(1 - \frac{p_{CH_4} p_{H_2O}}{p_{CO} p_{H_2}^3 K_{eq3}}\right)}{\left(1 + \sqrt{K_{H_2} p_{H_2}} + K_{CO_2} p_{CO_2}\sqrt{K_{H_2} p_{H_2}} + K_{OH}\frac{p_{H_2O}}{p_{H_2}^{0.5}} + K_{CO} p_{CO}\right)^2} \quad (23)$$

where $K_{eq3}$ is the equilibrium constant of CO methanation calculated from Gibbs free energy difference among $CO_2$ methanation and RWGS reactions. Note that the adsorption constants are the same of that of H-assisted CO formation model (Eq. (19)), indicating that reaction rate is slowed by the same intermediates (MASI, most abundant surface intermediates). Then, given that the $CO_2$ conversion is the sum of $CH_4$ and CO yields, the rate of CO formation is defined as:

$$r_{CO} = (-r_{CO_2}) - r_{CH_4} \quad (24)$$

Fig. 7 depicts the parity plot of all experimental $CO_2$ conversion points against the calculated/predicted ones, including the datasets in which partial pressure effect of $CO_2$ (blue), $H_2$ (red), $CH_4$ (green) and $H_2O$ (blue) was studied.

After incorporation of new points, the prediction accuracy of the model was similar to that above observed, presenting a remarkable low mean deviation of 7.0 %. Unfortunately, it can be noticed (see inset graph) that the model does not predict so well the $CO_2$ conversion in the low activity region ($X_{CO_2} < 20$ %), observing a general deviation of 30 % or even higher when different concentrations of products are fed. In fact, the model poorly predicts the effect of $H_2O$ at 325 °C. However, in the high activity region ($X_{CO_2} > 20$ %), most experimental points are within the ± 10 % region and the model predicts with high significance both the inhibiting effect of water and the insensitivity to $p_{CH_4}$ at 430 °C ($P = 2$ or 6 bar). Therefore, the satisfactory prediction under integral reactor conditions, which is the region of greatest interest for the industrial practice, proves that the model still is adequate.

The regressed constants of the elected mechanistic models (Eq (23)) are listed in Table 4 at different temperatures. Note that the kinetic constants of CO methanation rate are one order of magnitude higher than those of reverse water gas shift, indicating that the former is much faster. Furthermore, the relative high value of adsorption constants verifies that reaction rates are clearly influenced by adsorbed reaction intermediates except for $H_2$, whose adsorption constant value is not significantly different to zero and; therefore, it can be neglected. Note that the adsorption constant of CO is at least one order of magnitude higher than the rest, suggesting that adsorbed carbonyls have even more inhibiting effect than water or hydroxyls. On the other hand, the activation energy for $CO_2$ hydrogenation obtained by regression was similar to the apparent one calculated in Section 4.3.1 (91.6 vs. 80.1 kJ mol$^{-1}$), whereas that of CO methanation resulted in 26.3 kJ mol$^{-1}$. Regarding the adsorption enthalpies defined in Van't Hoff expression (Eq. (10)), those were – 7.86, – 26.0 and – 43.2 kJ mol$^{-1}$ for formate ($\Delta H_{HCOO}$), hydroxyls ($\Delta H_{OH}$), and CO ($\Delta H_{CO}$) adsorption, respectively. It must be highlighted that the adsorption constants fulfil the Boudart rules, according to which the entropy change of any adsorption must be negative ($\Delta S < 0$, i.e., more ordered state) and within the range:

$$10 < \Delta S < 12.2 - 0.0014\Delta H \quad (25)$$

Thus, Boudart rules verification and entropy change calculation were done applying Van't Hoff equation together with Gibbs function ($\Delta G^\circ = \Delta H^\circ - T\Delta S^\circ$), which derives in the following equation:

$$\ln(K) = -\frac{\Delta H^\circ}{RT} + \frac{\Delta S^\circ}{R}; \quad \Delta S^\circ = R\cdot\ln(K) + \frac{\Delta H^\circ}{RT} \quad (26)$$

The calculated entropy values fulfilled Boudart rules (Eq (25)) for formates ($\Delta S_{HCOO} = -20.4$ J mol$^{-1}$), hydroxyls ($\Delta S_{OH} = -30.4$ J mol$^{-1}$) and CO adsorption ($\Delta S_{CO} = -30.9$ J mol$^{-1}$). Noteworthy, formates present the lowest entropy value, which suggests that are the less stable species. Note that both hydroxyls and carbonyls present an entropy value 10 J mol$^{-1}$ higher, confirming that they are the species mainly inhibiting $CO_2$ methanation rate.

#### 4.4.1. H-assisted CO formation model validation

Fig. 8 plots a comparison of experimental (points) and predicted (lines) $CO_2$ conversion as a function of (a) reaction temperature as well as space-time, (b) $H_2$ to $CO_2$ ratio, (c) total pressure and (d) $H_2O$ partial pressure at the reactor inlet. In line with the determined in Figs. 4 and 5, the model predicts well the positive effect of temperature, space time ($W/F_{A0}$), pressure ($P$) and $H_2/CO_2$ on $CO_2$ conversion. On the contrary, feeding $H_2O$ has an inhibitory effect on reaction rate (see Fig. 4d), which also leads to a $CO_2$ conversion decrease at reactor outlet (Fig. 8d). It will be crucial that the inhibiting effect of products is adequately represented by the model for industrial scale application, since water contents at the reactor exit would range in excess of 50 mol%. Hence, all models parameterized on basis of reaction rates in absence of product gases would fail in this respect. Reported results in Fig. 4d demonstrate that the developed model can accurately estimate the effect of reagents and products partial pressures.

For further validation, the experimental light-off curve, obtained with a feed composition of 16 % of $CO_2$, 64 % of $H_2$ and 20 % of $N_2$ (total flowrate of 250 cm$^3$ min$^{-1}$) and total pressure of 1 bar, is compared with that predicted by the H-assisted CO formation model in the 200−500 °C temperature range (Fig. 9). As can be observed, the conversion is predicted adequately over the whole temperature range, which further validates the proposed model in this study.

In summary, since kinetic equations fit quite well experimental data (153 measurements) and all kinetic parameters have physical sense, H-assisted CO formation model, proposed for the first time in the present study, was validated to describe intrinsic kinetics on 9.5 wt.% $Ni/Al_2O_3$ catalyst under wide range of operational conditions.

## 5. Conclusions

The kinetic data included in this study show that the proposed LHHW mechanistic model, developed through a discrimination procedure, is capable to provide an excellent description of the intrinsic kinetics of $CO_2$ methanation over 9.5 wt.% $Ni/Al_2O_3$ catalyst. The chosen rate equations system, which is the one that best fits the kinetic data, assumes formate species decomposition into carbonyls via H-assisted CO formation mechanism (and further carbonyls hydrogenation into CHO) as rate determining step. In fact, this model, which covers a wide range of operating conditions from differential ($X_{CO_2} < 10$ %) to equilibrium ($X_{CO_2} > 80$ %) reactor, can predict satisfactorily the dependence of $CO_2$ hydrogenation rate with reagents partial pressure ($p_{CO_2}$ and $p_{H_2}$), the boosting effect of temperature, as well as $H_2/CO_2$ molar ratio in the feedstream on the $CO_2$ conversion. Furthermore, the inhibitory effect of strongly adsorbed $OH^-$ and CO surface intermediates is well predicted. Noteworthy, its mean absolute deviation ($D$= 7.0 %) is significantly lower to that of the model most employed in literature to describe the kinetics of Ni-Al formulation with higher Ni contents ($D = 20$ %), which considers that associative hydrogenation of adsorbed CO formed from direct $CO_2$ dissociation is the RDS. This work confirms that not only carbonyls but also formate species participate in the $CO_2$ methanation mechanism and concludes that it has an important role in kinetics of lowly-loaded $Ni/Al_2O_3$ catalyst.

## Data availability

No data was used for the research described in the article.

## CRediT authorship contribution statement

**A. Quindimil:** Conceptualization, Data curation, Investigation, Methodology, Validation. Visualization, Writing – original draft. **J. A. Onrubia-Calvo:** Conceptualization, Data curation, Methodology, Visualization, Writing – review & editing. **A. Davó-Quiñonero:** Methodology (catalyst synthesis and characterization), Writing – review & editing. **A. Bermejo-López:** Data curation, Methodology, Visualization, review & editing. **E. Bailón-García:** Methodology (catalyst synthesis and characterization), Writing – review & editing. **B. Pereda-Ayo:** Conceptualization, Data curation, Methodology, Visualization, review & editing. **Dolores Lozano Castelló:** Funding adquisition, Validation, Writing – review & editing. **J. A. González-Marcos:** Funding acquisition, Formal analysis, Resources, Software. **A. Bueno-López:** Funding adquisition, Validation, Writing – review & editing. **J. R. González-Velasco:** Conceptualization, Funding acquisition, Project administration, Resources, Supervision, Writing – review & editing.

## Declaration of Competing Interest

The authors declare that they have no known competing financial interests or personal relationships that could have appeared to influence the work reported in this paper.

## Acknowledgements

Support for this study was provided by the Spanish Ministry of Economy and Competiveness (Project PID2019-105960RB-C21 and PID2019-105960RB-C22) and the Basque Government (Project IT1297-19). One of the authors (JAOC) acknowledges the Post-doctoral research grant (DOCREC20/49) provided by the University of the Basque Country. Other of the authors (AQ) also acknowledges University of the Basque Country by his PhD grant (PIF-15/351).

## Appendix A

### *A1 Assessment of heat transfer limitations*

In order to assess heat transfer limitation Anderson's and Mear's criteria are employed. For both criteria, initial reaction rates ($-r^0_{CO_2}$) in Table S2 are inserted as observed reaction rates $r_A^{obs}$ in mol $kg^{-1}$ $s^{-1}$ and the activation energy ($E_A$) is considered similar to the apparent one ($E_{ap}$) expressed in kJ $mol^{-1}$.

Intraparticle heat transport can be ignored if the Anderson's criterion is fulfilled:

$$\frac{\left(-r_A^{obs}\right)\cdot|\Delta H_{Rx}|\cdot\rho_{cat}\cdot r_{cat}^2}{\lambda\cdot T} < \frac{0.75\cdot R\cdot T}{E_A} \tag{A1.1}$$

where $\Delta H_{RX}$ is the reaction heat (kJ $mol^{-1}$), $\rho_{cat}$ is the solid density of catalyst pellet (kg $m^{-3}$), $r_{cat}$ is the radios of catalyst pellet (m), $\lambda$ is the thermal conductivity of the gas phase approximated by the rule of Wassiljeva (kW $m^{-1}$ $K^{-1}$) and R is the ideal gas constant (8.31 $10^{-3}$ kJ $mol^{-1}$ $K^{-1}$)

External heat transfer limitation can be neglected if the Mears' criterion is satisfied:

$$\frac{\left(-r_A^{obs}\right)\cdot\rho_b\cdot r_{cat}\cdot E_{ap}\cdot|\Delta H_{Rx}|}{h\cdot T^2\cdot R} < 0.15 \tag{A1.2}$$

where $\rho_b$ is the bulk density of the catalyst bed (kg $m^{-3}$) and $h$ is the heat transfer coefficient between gas and pellet (kW $m^{-2}$ $s^{-1}$) calculated assuming that Nusselt number is 2, since the Reynolds number for this system is much smaller than 1.

### *A2 Derivation of LHHW kinetic rate equation from dissociative CO formation mechanism*

The kinetic rate equation is derived analogously to the methodology of reference [39] and from mechanism proposed in Table 2. The $CO_2$ disappearance rate is equal to the rate of elementary step 4 (formation of formyl species), which is considered as rate determining step:

$$-r_{CO_2} = r_4 = k_4\Theta_{CO}\Theta_H \tag{A2.1}$$

where $\Theta_{CO}$ and $\Theta_H$ are the coverages of hydrogen and carbonyl and $k_4$ is the forward kinetic constant of elementary step 4.

The coverage of hydrogen is easily derived by assuming dissociative Langmuir adsorption in quasi-equilibrium:

$$k_1 p_{H_2}\Theta_*^2 = k_{-1}\Theta_H \tag{A2.2}$$

$$\Theta_H = \sqrt{\frac{k_1}{k_{-1}}p_{H_2}\Theta_*^2} = \sqrt{K_1 p_{H_2}}\Theta_* \tag{A2.3}$$

where $K_1$ is the equilibrium constant of step 1 and $\Theta_*$ is the fraction of free active sites. On the other hand, carbonyls arise from dissociative adsorption of $CO_2$, which is also assumed as Langmuir adsorption in quasi-equilibrium.

$$k_2 p_{CO_2}\Theta_*^2 = k_{-2}\Theta_{CO}\Theta_O \tag{A2.4}$$

$$\Theta_{CO} = \frac{k_2}{k_{-2}}\frac{p_{CO_2}\Theta_*^2}{\Theta_O} = K_2\frac{p_{CO_2}\Theta_*^2}{\Theta_O} \tag{A2.5}$$

At steady state, the oxygen hydrogenation rate (step 8) is two times the rate of carbonyls hydrogenation (RDS). Then,

$$r_8 = k_8\Theta_O\Theta_H = 2(-r_{CO_2}) = 2k_3\Theta_O\Theta_H \tag{A2.6}$$

and the oxygen coverage can be expressed as function of carbonyls coverage:

$$\Theta_O = \frac{2k_3\Theta_{CO}}{k_6} \tag{A2.7}$$

Inserting Eq. (A2.7) in Eq. (A2.5), CO coverage finally results in:

$$\Theta_{CO} = K_2\frac{p_{CO_2}\Theta_*^2}{2k_4\Theta_{CO}/k_8} \rightarrow \Theta_{CO}^2 = K_2\frac{p_{CO_2}\Theta_*^2 k_8}{2k_4} \rightarrow \Theta_{CO} = \sqrt{\frac{K_2k_8}{2k_4}p_{CO_2}}\Theta_* \tag{A2.8}$$

Thus, the reaction rate can be expressed as:

$$-r_{CO_2} = k_4\Theta_{CO}\Theta_H = k_4\sqrt{\frac{K_2k_8}{2k_4}p_{CO_2}}\Theta_*\sqrt{K_1p_{H_2}}\Theta_* = k_4\sqrt{\frac{K_2k_8K_1}{2k_4}p_{CO_2}p_{H_2}}\Theta_*^2 \tag{A2.9}$$

Assuming that dissociated hydrogen atoms, carbonyls and hydroxyls are the most abundant surface intermediates (MASI) the balance of active sites can be formulated as follows:

$$1 = \Theta_* + \Theta_H + \Theta_{CO} + \Theta_{OH} \tag{A2.10}$$

$$\Theta_{CO}^2 = K_2\frac{p_{CO_2}\Theta_*^2 k_8}{2k_4} \rightarrow \Theta_{CO} = \sqrt{\frac{K_2k_8}{2k_4}p_{CO_2}}\Theta_* \tag{A2.11}$$

Considering that steps 9 and 10 are in equilibrium the hydroxyl coverage can be expressed as:

$$k_9\Theta_{OH}\Theta_H = k_{-9}\Theta_{H_2O}\Theta_* \rightarrow \Theta_{OH} = \frac{k_{-9}}{k_9}\frac{\Theta_{H_2O}\Theta_*}{\Theta_H} = \frac{\Theta_{H_2O}}{K_9\sqrt{K_1p_{H_2}}} \tag{A2.12}$$

where the water coverage can be expressed as function of water partial pressure:

$$k_{10}\Theta_{H_2O} = k_{-10}p_{H_2O} \rightarrow \Theta_{H_2O} = \frac{k_{-10}}{k_{10}}p_{H_2O}\Theta_* = \frac{p_{H_2O}}{K_{10}}\Theta_* \tag{A2.13}$$

Then, the hydroxyl coverage is defined as:

$$\Theta_{OH} = \frac{p_{H_2O}\Theta_*}{K_9K_{10}\sqrt{K_1p_{H_2}}} \tag{A2.14}$$

Introducing Eqs. (A2.3), (A2.8) and (A2.15) in Eq. (A2.11), the fraction of free active sites can be formulated as function of known variables:

$$1 = \Theta_* + \sqrt{K_1p_{H_2}}\Theta_* + \sqrt{\frac{K_2k_8}{2k_4}p_{CO_2}}\Theta_* + \frac{p_{H_2O}\Theta_*}{K_9K_{10}\sqrt{K_1p_{H_2}}} \tag{A2.15}$$

$$\Theta_* = \frac{1}{1 + \sqrt{K_1p_{H_2}} + \sqrt{\frac{K_2k_8}{2k_4}p_{CO_2}} + \frac{p_{H_2O}}{K_{10}K_9\sqrt{K_1p_{H_2}}}} \tag{A2.16}$$

Finally, considering thermodynamic equilibrium, the reaction rate results in:

$$-r_{CO_2} = \frac{k_4\sqrt{\frac{K_2k_8K_1}{2k_4}p_{CO_2}p_{H_2}}}{\left(1 + \sqrt{K_1p_{H_2}} + \sqrt{\frac{K_2k_8}{2k_4}p_{CO_2}} + \frac{p_{H_2O}}{K_{10}K_9\sqrt{K_1p_{H_2}}}\right)^2} \tag{A2.17}$$

Grouping constants in convenience, the reaction rate is expressed as:

$$-r_{CO_2} = \frac{k_4p_{CO_2}^{0.5}p_{H_2}^{0.5}\left(1 - \frac{p_{CH_4}p_{H_2O}^2}{p_{CO_2}p_{H_2}^4K_{Eq1}}\right)}{\left(1 + \sqrt{K_{H_2}p_{H_2}} + \sqrt{K_{CO_2}p_{CO_2}} + K_{OH}\frac{p_{H_2O}}{p_{H_2}^{0.5}}\right)^2} \tag{A2.18}$$

### *A3 Derivation of LHHW kinetic rate equations from H-assisted CO formation mechanism*

The $CO_2$ disappearance rate equation as well as $CH_4$ and CO formation rates equations are deduced from H-assisted CO formation mechanism proposed in Table 3. The $CO_2$ disappearance rate is equal to the rate of elementary step 4 (decomposition of formates into CO).

$$-r_{CO_2} = r_4 = k_4\Theta_{HCOO}\Theta_* \tag{A3.1}$$

Considering that Langmuir $H_2$ adsorption (step 1) is in quasi-equilibrium, the $H_2$ coverage can be expressed as:

$$k_1p_{H_2}\Theta_*^2 = k_{-1}\Theta_H \rightarrow \Theta_H = \sqrt{\frac{k_1}{k_{-1}}p_{H_2}\Theta_*^2} = \sqrt{K_1p_{H_2}}\Theta_* \tag{A3.2}$$

According to this mechanism, $CO_2$ is molecularly adsorbed on OH– groups of $Al_2O_3$ in form of bicarbonates (step 2), which are further

hydrogenated into formates (step 3). Assuming that step 2 and 3 are also in quasi-equilibrium, the bicarbonates coverage is easily accessible:

$$k_2 p_{CO_2} \Theta_{OH} = k_{-2} \Theta_{HCO_3} \rightarrow \Theta_{HCO_3} = \frac{k_2}{k_{-2}} p_{CO_2} \Theta_{OH} = K_2 p_{CO_2} \Theta_{OH} \tag{A3.3}$$

and the formates coverage:

$$k_3 \Theta_{HCO_3} \Theta_H = k_{-3} \Theta_{HCOO} \Theta_{OH} \rightarrow \Theta_{HCOO} = \frac{k_3}{k_{-3}} \frac{\Theta_{HCO_3} \Theta_H}{\Theta_{OH}} = K_3 \frac{\Theta_{HCO_3} \Theta_H}{\Theta_{OH}} \tag{A3.4}$$

which after inserting the coverage of hydrogen (Eq. (A3.2)) and bicarbonates (Eq. (A3.4)) results in:

$$\Theta_{HCOO} = \frac{K_2 K_3 p_{CO_2} \Theta_{OH} \sqrt{K_1 p_{H_2}} \Theta_*}{\Theta_{OH}} = K_2 K_3 p_{CO_2} \sqrt{K_1 p_{H_2}} \Theta_* \tag{A3.5}$$

Then, replacing formates coverage in Eq. (A3.1) the rate equation can be formulated as:

$$-r_{CO_2} = k_4 K_2 K_3 \sqrt{K_1} p_{CO_2} \sqrt{p_{H_2}} \Theta_*^2 \tag{A3.6}$$

Assuming that hydrogen dissociated atoms, formates, carbonyls and hydroxyls occupy most of the active sites, the active sites balance is expressed as:

$$1 = \Theta_* + \Theta_H + \Theta_{HCOO} + \Theta_{CO} + \Theta_{OH} \tag{A3.7}$$

The carbonyls coverage is derived from step 5 in quasi-equilibrium:

$$k_5 \Theta_{CO} = k_{-5} p_{CO} \Theta_* \rightarrow \Theta_{CO} = \frac{k_{-5}}{k_5} p_{CO} \Theta_* = \frac{p_{CO}}{K_5} \Theta_* \tag{A3.8}$$

whereas the coverage of hydroxyls is derived assuming step 11 in quasi-equilibrium and low $H_2O$ coverage in step 12

$$k_{11} \Theta_{OH} \Theta_H = k_{-11} \Theta_{H_2O} \Theta_* \rightarrow \Theta_{OH} = \frac{k_{-11}}{k_{11}} \frac{\Theta_{H_2O} \Theta_*}{\Theta_H} = \frac{\Theta_{H_2O}}{K_{11} \sqrt{K_1 p_{H_2}}} \tag{A3.9}$$

where the water coverage can be expressed as function of water partial pressure:

$$k_{12} \Theta_{H_2O} = k_{-12} p_{H_2O} \rightarrow \Theta_{H_2O} = \frac{k_{-12}}{k_{12}} p_{H_2O} \Theta_* = \frac{p_{H_2O}}{K_{12}} \Theta_* \tag{A3.10}$$

Then, the hydroxyl coverage is defined as:

$$\Theta_{OH} = \frac{p_{H_2O} \Theta_*}{K_{11} K_{12} \sqrt{K_1 p_{H_2}}} \tag{A3.11}$$

Introducing Eqs. (A3.2), (A3.7), (A3.9) and (A3.12) in Eq. (A3.8), the fraction of free active sites can be formulated as function of known variables:

$$1 = \Theta_* + \sqrt{K_1 p_{H_2}} \Theta_* + K_2 K_3 p_{CO_2} \sqrt{K_1 p_{H_2}} \Theta_* + \frac{p_{CO}}{K_5} \Theta_* + \frac{p_{H_2O} \Theta_*}{K_{11} K_{12} \sqrt{K_1 p_{H_2}}} \tag{A3.12}$$

$$\Theta_* = \frac{1}{1 + \sqrt{K_1 p_{H_2}} + K_2 K_3 p_{CO_2} \sqrt{K_1 p_{H_2}} + \frac{p_{CO}}{K_5} + \frac{p_{H_2O}}{K_{11} K_{12} \sqrt{K_1 p_{H_2}}}} \tag{A3.13}$$

Considering thermodynamic equilibrium of RWGS the reaction rate is written as:

$$-r_{CO_2} = \frac{k_4 K_2 K_3 \sqrt{K_1} p_{CO_2} \sqrt{p_{H_2}} \left(1 - \frac{p_{CO} p_{H_2O}}{p_{CO_2} p_{H_2} K_{eq2}}\right)}{\left(1 + \sqrt{K_1 p_{H_2}} + K_2 K_3 p_{CO_2} \sqrt{K_1 p_{H_2}} + \frac{p_{CO}}{K_5} + \frac{p_{H_2O}}{K_{11} K_{12} \sqrt{K_1 p_{H_2}}}\right)^2} \tag{A3.14}$$

which, after grouping adsorption constants for convenience results in:

$$-r_{CO_2} = \frac{k_4 p_{CO_2} p_{H_2}^{0.5} \left(1 - \frac{p_{CO} p_{H_2O}}{p_{CO_2} p_{H_2} K_{eq2}}\right)}{\left(1 + \sqrt{K_{H_2} p_{H_2}} + K_{CO_2} p_{CO_2} \sqrt{K_{H_2} p_{H_2}} + K_{OH} \frac{p_{H_2O}}{p_{H_2}^{0.5}} + K_{CO} p_{CO}\right)^2} \tag{A3.15}$$

On the other hand, the rate of $CH_4$ formation is considered the same as that of step 6 (formation of formyl species):

$$r_{CH_4} = r_6 = k_6 \Theta_{CO} \Theta_H \tag{A3.16}$$

Inserting the coverages of carbonyl (Eq. (A3.9)) and hydrogen (Eq. (A3.2)) defined above, the $CH_4$ formation rate is expressed as:

**Table A4**
Kinetic measurements operational conditions and data pool.

| Experiment | P, bar | T, °C | $W/F^0_{CO_2}$, g h mol$^{-1}$ | $\varepsilon_A$[a] | $p^{in}_{CO_2}$, bar | H/C[b] | M/C[c] | A/C[d] | $X_{CO_2}$, % | $Y_{CH_4}$, % |
|---|---|---|---|---|---|---|---|---|---|---|
| 1 | 2 | 325 | 24.89 | −0.06 | 0.06 | 0 | 0 | 0 | 20.8 | 19.5 |
| 2 | 2 | 325 | 15.56 | −0.10 | 0.10 | 0 | 0 | 0 | 14.3 | 13.3 |
| 3 | 2 | 325 | 12.44 | −0.12 | 0.12 | 0 | 0 | 0 | 12.3 | 11.2 |
| 4 | 2 | 325 | 6.22 | −0.24 | 0.24 | 0 | 0 | 0 | 7.4 | 6.4 |
| 5 | 2 | 325 | 4.67 | −0.32 | 0.32 | 0 | 0 | 0 | 5.9 | 5 |
| 6 | 2 | 325 | 3.11 | −0.48 | 0.48 | 0 | 0 | 0 | 4.4 | 3.6 |
| 7 | 2 | 325 | 12.44 | −0.12 | 0.12 | 0 | 0 | 0 | 6.9 | 4.8 |
| 8 | 2 | 325 | 12.44 | −0.12 | 0.12 | 0 | 0 | 0 | 8.5 | 6.7 |
| 9 | 2 | 325 | 12.44 | −0.12 | 0.12 | 0 | 0 | 0 | 9.4 | 7.9 |
| 10 | 2 | 325 | 12.44 | −0.12 | 0.12 | 0 | 0 | 0 | 10.3 | 8.8 |
| 11 | 2 | 325 | 12.44 | −0.12 | 0.12 | 0 | 0 | 0 | 10.7 | 9.4 |
| 12 | 2 | 325 | 12.44 | −0.12 | 0.12 | 0 | 0 | 0 | 11 | 9.8 |
| 13 | 2 | 325 | 9.33 | −0.16 | 0.16 | 4 | 0.35 | 0 | 6.7 | 5.6 |
| 14 | 2 | 325 | 9.33 | −0.16 | 0.16 | 4 | 0.7 | 0 | 5.7 | 4.6 |
| 15 | 2 | 325 | 9.33 | −0.16 | 0.16 | 4 | 1.05 | 0 | 6 | 4.9 |
| 16 | 2 | 325 | 9.33 | −0.16 | 0.16 | 4 | 1.7 | 0 | 5.5 | 4.3 |
| 17 | 2 | 325 | 9.33 | −0.16 | 0.16 | 4 | 2.05 | 0 | 4.8 | 3.6 |
| 18 | 2 | 325 | 9.33 | −0.16 | 0.16 | 4 | 0 | 0.25 | 7.4 | 6.3 |
| 19 | 2 | 325 | 9.33 | −0.16 | 0.16 | 4 | 0 | 1.25 | 3.9 | 3 |
| 20 | 2 | 325 | 9.33 | −0.16 | 0.16 | 4 | 0 | 1.75 | 3.9 | 3 |
| 21 | 2 | 325 | 9.33 | −0.16 | 0.16 | 4 | 0 | 2.25 | 3.6 | 2.7 |
| 22 | 2 | 325 | 9.33 | −0.16 | 0.16 | 4 | 0 | 3.00 | 3.2 | 2.4 |
| 23 | 2 | 325 | 9.33 | −0.16 | 0.16 | 4 | 0 | 3.75 | 2.8 | 2.1 |
| 24 | 2 | 325 | 9.33 | −0.32 | 0.32 | 4 | 0 | 0 | 10.1 | 9 |
| 25 | 2 | 325 | 9.33 | −0.27 | 0.27 | 4 | 0 | 0 | 9.6 | 8.4 |
| 26 | 2 | 325 | 9.33 | −0.20 | 0.20 | 4 | 0 | 0 | 8.8 | 7.6 |
| 27 | 2 | 325 | 9.33 | −0.16 | 0.16 | 4 | 0 | 0 | 8.3 | 7 |
| 28 | 2 | 325 | 9.33 | −0.11 | 0.11 | 4 | 0 | 0 | 7.6 | 6.1 |
| 29 | 2 | 325 | 9.33 | −0.08 | 0.08 | 4 | 0 | 0 | 7.9 | 5.9 |
| 30 | 2 | 315 | 3.39 | −0.20 | 0.20 | 4 | 0 | 0 | 3.2 | 2.6 |
| 31 | 2 | 315 | 3.73 | −0.20 | 0.20 | 4 | 0 | 0 | 3.5 | 2.8 |
| 32 | 2 | 315 | 4.67 | −0.20 | 0.20 | 4 | 0 | 0 | 4 | 3.3 |
| 33 | 2 | 315 | 6.22 | −0.20 | 0.20 | 4 | 0 | 0 | 4.8 | 4 |
| 34 | 2 | 315 | 9.33 | −0.20 | 0.20 | 4 | 0 | 0 | 6.5 | 5.8 |
| 35 | 2 | 315 | 18.67 | −0.20 | 0.20 | 4 | 0 | 0 | 10.5 | 9.7 |
| 36 | 2 | 335 | 3.39 | −0.20 | 0.20 | 4 | 0 | 0 | 5.4 | 4.3 |
| 37 | 2 | 335 | 3.73 | −0.20 | 0.20 | 4 | 0 | 0 | 5.8 | 4.7 |
| 38 | 2 | 335 | 4.67 | −0.20 | 0.20 | 4 | 0 | 0 | 6.7 | 5.4 |
| 39 | 2 | 335 | 6.22 | −0.20 | 0.20 | 4 | 0 | 0 | 7.8 | 6.6 |
| 40 | 2 | 335 | 9.33 | −0.20 | 0.20 | 4 | 0 | 0 | 10.5 | 9.2 |
| 41 | 2 | 335 | 18.67 | −0.20 | 0.20 | 4 | 0 | 0 | 16.5 | 15.2 |
| 42 | 2 | 350 | 3.39 | −0.20 | 0.20 | 4 | 0 | 0 | 7.8 | 6.2 |
| 43 | 2 | 350 | 3.73 | −0.20 | 0.20 | 4 | 0 | 0 | 8.3 | 6.7 |
| 44 | 2 | 350 | 4.67 | −0.20 | 0.20 | 4 | 0 | 0 | 9.5 | 7.7 |
| 45 | 2 | 350 | 6.22 | −0.20 | 0.20 | 4 | 0 | 0 | 11.2 | 9.3 |
| 46 | 2 | 350 | 9.33 | −0.20 | 0.20 | 4 | 0 | 0 | 14.8 | 13 |
| 47 | 2 | 350 | 18.67 | −0.20 | 0.20 | 4 | 0 | 0 | 22.8 | 21 |
| 48 | 2 | 355 | 3.39 | −0.20 | 0.20 | 4 | 0 | 0 | 8.8 | 7 |
| 49 | 2 | 355 | 3.73 | −0.20 | 0.20 | 4 | 0 | 0 | 9.3 | 7.4 |
| 50 | 2 | 355 | 4.67 | −0.20 | 0.20 | 4 | 0 | 0 | 10.6 | 8.5 |
| 51 | 2 | 355 | 6.22 | −0.20 | 0.20 | 4 | 0 | 0 | 12.6 | 10.5 |
| 52 | 2 | 355 | 9.33 | −0.20 | 0.20 | 4 | 0 | 0 | 16.6 | 14.5 |
| 53 | 2 | 355 | 18.67 | −0.20 | 0.20 | 4 | 0 | 0 | 25.4 | 23.4 |
| 54 | 2 | 370 | 3.39 | −0.20 | 0.20 | 4 | 0 | 0 | 10.8 | 7.8 |
| 55 | 2 | 370 | 3.73 | −0.20 | 0.20 | 4 | 0 | 0 | 11.4 | 8.3 |
| 56 | 2 | 370 | 4.67 | −0.20 | 0.20 | 4 | 0 | 0 | 12.8 | 9.4 |
| 57 | 2 | 370 | 6.22 | −0.20 | 0.20 | 4 | 0 | 0 | 15 | 11.6 |
| 58 | 2 | 370 | 9.33 | −0.20 | 0.20 | 4 | 0 | 0 | 19.2 | 15.9 |
| 59 | 2 | 370 | 18.67 | −0.20 | 0.20 | 4 | 0 | 0 | 28.2 | 25.1 |
| 60 | 2 | 390 | 3.39 | −0.20 | 0.20 | 4 | 0 | 0 | 16 | 11.4 |
| 61 | 2 | 390 | 3.73 | −0.20 | 0.20 | 4 | 0 | 0 | 16.8 | 12.1 |
| 62 | 2 | 390 | 4.67 | −0.20 | 0.20 | 4 | 0 | 0 | 18.6 | 13.5 |
| 63 | 2 | 390 | 6.22 | −0.20 | 0.20 | 4 | 0 | 0 | 21.8 | 16.6 |
| 64 | 2 | 390 | 9.33 | −0.20 | 0.20 | 4 | 0 | 0 | 27.5 | 22.5 |
| 65 | 2 | 390 | 18.67 | −0.20 | 0.20 | 4 | 0 | 0 | 38.1 | 34 |
| 66 | 2 | 410 | 3.39 | −0.20 | 0.20 | 4 | 0 | 0 | 22.7 | 15.9 |
| 67 | 2 | 410 | 3.73 | −0.20 | 0.20 | 4 | 0 | 0 | 23.7 | 16.7 |
| 68 | 2 | 410 | 4.67 | −0.20 | 0.20 | 4 | 0 | 0 | 26 | 18.6 |
| 69 | 2 | 410 | 6.22 | −0.20 | 0.20 | 4 | 0 | 0 | 29.8 | 22.5 |
| 70 | 2 | 410 | 9.33 | −0.20 | 0.20 | 4 | 0 | 0 | 36.6 | 30 |
| 71 | 2 | 410 | 18.67 | −0.20 | 0.20 | 4 | 0 | 0 | 48 | 43.6 |
| 72 | 2 | 430 | 3.39 | −0.20 | 0.20 | 4 | 0 | 0 | 30.6 | 21.3 |
| 73 | 2 | 430 | 3.73 | −0.20 | 0.20 | 4 | 0 | 0 | 31.7 | 22.2 |
| 74 | 2 | 430 | 4.67 | −0.20 | 0.20 | 4 | 0 | 0 | 34.7 | 24.8 |

(*continued on next page*)

**Table A4** (*continued*)

| Experiment | P, bar | T, °C | $W/F^0_{CO_2}$, g h mol$^{-1}$ | $\varepsilon_A$[a] | $p^{in}_{CO_2}$, bar | H/C[b] | M/C[c] | A/C[d] | $X_{CO_2}$, % | $Y_{CH_4}$, % |
|---|---|---|---|---|---|---|---|---|---|---|
| 75 | 2 | 430 | 6.22 | −0.20 | 0.20 | 4 | 0 | 0 | 38.9 | 29.7 |
| 76 | 2 | 430 | 9.33 | −0.20 | 0.20 | 4 | 0 | 0 | 45.4 | 38.1 |
| 77 | 2 | 430 | 18.67 | −0.20 | 0.20 | 4 | 0 | 0 | 55.6 | 51.6 |
| 78 | 4 | 430 | 3.73 | −0.20 | 0.40 | 4 | 0 | 0 | 38.5 | 32.7 |
| 79 | 4 | 430 | 4.67 | −0.20 | 0.40 | 4 | 0 | 0 | 43 | 37.9 |
| 80 | 4 | 430 | 6.22 | −0.20 | 0.40 | 4 | 0 | 0 | 49.3 | 45.1 |
| 81 | 4 | 430 | 9.33 | −0.20 | 0.40 | 4 | 0 | 0 | 58.2 | 55.3 |
| 82 | 4 | 430 | 12.44 | −0.20 | 0.40 | 4 | 0 | 0 | 63.8 | 61.7 |
| 83 | 4 | 430 | 18.67 | −0.20 | 0.40 | 4 | 0 | 0 | 68.7 | 67.3 |
| 84 | 6 | 430 | 3.73 | −0.20 | 0.60 | 4 | 0 | 0 | 41.4 | 37.3 |
| 85 | 6 | 430 | 4.67 | −0.20 | 0.60 | 4 | 0 | 0 | 46.9 | 43.4 |
| 86 | 6 | 430 | 6.22 | −0.20 | 0.60 | 4 | 0 | 0 | 54.8 | 52 |
| 87 | 6 | 430 | 9.33 | −0.20 | 0.60 | 4 | 0 | 0 | 64.3 | 62.5 |
| 88 | 6 | 430 | 12.44 | −0.20 | 0.60 | 4 | 0 | 0 | 69.3 | 68 |
| 89 | 6 | 430 | 18.67 | −0.20 | 0.60 | 4 | 0 | 0 | 72.9 | 72 |
| 90 | 2 | 430 | 24.89 | −0.06 | 0.06 | 16 | 0 | 0 | 91.4 | 89.9 |
| 91 | 2 | 430 | 18.67 | −0.08 | 0.08 | 12 | 0 | 0 | 82.7 | 80 |
| 92 | 2 | 430 | 15.56 | −0.10 | 0.10 | 10 | 0 | 0 | 75.8 | 72.2 |
| 93 | 2 | 430 | 12.44 | −0.12 | 0.12 | 8 | 0 | 0 | 67.8 | 63.5 |
| 94 | 2 | 430 | 6.22 | −0.24 | 0.24 | 4 | 0 | 0 | 44.6 | 38.2 |
| 95 | 2 | 430 | 4.67 | −0.32 | 0.32 | 3 | 0 | 0 | 37 | 30 |
| 96 | 2 | 430 | 12.44 | −0.12 | 0.12 | 1 | 0 | 0 | 20.1 | 10.4 |
| 97 | 2 | 430 | 12.44 | −0.12 | 0.12 | 2 | 0 | 0 | 31 | 21.7 |
| 98 | 2 | 430 | 12.44 | −0.12 | 0.12 | 3 | 0 | 0 | 40 | 31.5 |
| 99 | 2 | 430 | 12.44 | −0.12 | 0.12 | 4 | 0 | 0 | 47.5 | 39.9 |
| 100 | 2 | 430 | 12.44 | −0.12 | 0.12 | 5 | 0 | 0 | 53.6 | 46.8 |
| 101 | 2 | 430 | 12.44 | −0.12 | 0.12 | 6 | 0 | 0 | 58.3 | 52.3 |
| 102 | 2 | 430 | 9.33 | −0.16 | 0.16 | 4 | 0.35 | 0 | 46.3 | 39.4 |
| 103 | 2 | 430 | 9.33 | −0.16 | 0.16 | 4 | 0.70 | 0 | 45.2 | 38 |
| 104 | 2 | 430 | 9.33 | −0.16 | 0.16 | 4 | 1.05 | 0 | 44.6 | 37.3 |
| 105 | 2 | 430 | 9.33 | −0.16 | 0.16 | 4 | 1.70 | 0 | 43 | 35.3 |
| 106 | 2 | 430 | 9.33 | −0.16 | 0.16 | 4 | 2.05 | 0 | 42.4 | 34.7 |
| 107 | 2 | 430 | 9.33 | −0.16 | 0.16 | 4 | 0 | 0.25 | 43.1 | 36.3 |
| 108 | 2 | 430 | 9.33 | −0.16 | 0.16 | 4 | 0 | 0.75 | 37.7 | 31.2 |
| 109 | 2 | 430 | 9.33 | −0.16 | 0.16 | 4 | 0 | 1.25 | 32.9 | 26.9 |
| 110 | 2 | 430 | 9.33 | −0.16 | 0.16 | 4 | 0 | 1.75 | 29 | 23.4 |
| 111 | 2 | 430 | 9.33 | −0.16 | 0.16 | 4 | 0 | 2.25 | 25.9 | 20.6 |
| 112 | 2 | 430 | 9.33 | −0.16 | 0.16 | 4 | 0 | 3.00 | 20.9 | 16.2 |
| 113 | 2 | 430 | 9.33 | −0.16 | 0.16 | 4 | 0 | 3.75 | 17.8 | 13.5 |
| 114 | 2 | 430 | 7.47 | −0.11 | 0.11 | 8 | 0 | 0 | 54.8 | 48.5 |
| 115 | 2 | 430 | 8.30 | −0.11 | 0.11 | 8 | 0 | 0 | 56 | 50.2 |
| 116 | 2 | 430 | 9.33 | −0.11 | 0.11 | 8 | 0 | 0 | 59.3 | 53.7 |
| 117 | 2 | 430 | 10.67 | −0.11 | 0.11 | 8 | 0 | 0 | 62.9 | 57.9 |
| 118 | 2 | 430 | 12.44 | −0.11 | 0.11 | 8 | 0 | 0 | 67.4 | 63 |
| 119 | 2 | 430 | 14.93 | −0.11 | 0.11 | 8 | 0 | 0 | 72 | 68.5 |
| 120 | 4 | 430 | 7.47 | −0.11 | 0.22 | 8 | 0 | 0 | 62.5 | 59.3 |
| 121 | 4 | 430 | 8.30 | −0.11 | 0.22 | 8 | 0 | 0 | 66.3 | 63.4 |
| 122 | 4 | 430 | 9.33 | −0.11 | 0.22 | 8 | 0 | 0 | 69.8 | 67.2 |
| 123 | 4 | 430 | 10.67 | −0.11 | 0.22 | 8 | 0 | 0 | 74.2 | 72 |
| 124 | 4 | 430 | 12.44 | −0.11 | 0.22 | 8 | 0 | 0 | 78 | 76.1 |
| 125 | 4 | 430 | 14.93 | −0.11 | 0.22 | 8 | 0 | 0 | 83.9 | 82.6 |
| 126 | 6 | 430 | 7.47 | −0.11 | 0.33 | 8 | 0 | 0 | 68.6 | 66.4 |
| 127 | 6 | 430 | 8.30 | −0.11 | 0.33 | 8 | 0 | 0 | 72.6 | 70.8 |
| 128 | 6 | 430 | 9.33 | −0.11 | 0.33 | 8 | 0 | 0 | 76.7 | 75.1 |
| 129 | 6 | 430 | 10.67 | −0.11 | 0.33 | 8 | 0 | 0 | 81.2 | 79.9 |
| 130 | 6 | 430 | 12.44 | −0.11 | 0.33 | 8 | 0 | 0 | 85.7 | 84.6 |
| 131 | 6 | 430 | 14.93 | −0.11 | 0.33 | 8 | 0 | 0 | 90.4 | 89.7 |
| 132 | 6 | 430 | 24.89 | −0.06 | 0.18 | 16 | 0 | 0 | 97 | 96.9 |
| 133 | 6 | 430 | 18.67 | −0.08 | 0.24 | 12 | 0 | 0 | 92.3 | 91.8 |
| 134 | 6 | 430 | 15.56 | −0.10 | 0.29 | 10 | 0 | 0 | 87.7 | 86.9 |
| 135 | 6 | 430 | 12.44 | −0.12 | 0.36 | 8 | 0 | 0 | 80.9 | 79.8 |
| 136 | 6 | 430 | 6.22 | −0.24 | 0.72 | 4 | 0 | 0 | 54.4 | 52.2 |
| 137 | 6 | 430 | 4.67 | −0.32 | 0.96 | 3 | 0 | 0 | 44.4 | 41.8 |
| 138 | 6 | 430 | 12.44 | −0.12 | 0.36 | 1 | 0 | 0 | 20.4 | 16.7 |
| 139 | 6 | 430 | 12.44 | −0.12 | 0.36 | 2 | 0 | 0 | 36.2 | 33 |
| 140 | 6 | 430 | 12.44 | −0.12 | 0.36 | 3 | 0 | 0 | 49.3 | 46.5 |
| 141 | 6 | 430 | 12.44 | −0.12 | 0.36 | 4 | 0 | 0 | 59.6 | 57.1 |
| 142 | 6 | 430 | 12.44 | −0.12 | 0.36 | 5 | 0 | 0 | 67.6 | 65.4 |
| 143 | 6 | 430 | 12.44 | −0.12 | 0.36 | 6 | 0 | 0 | 73.3 | 71.5 |
| 144 | 6 | 430 | 9.33 | −0.16 | 0.48 | 4 | 0 | 0.25 | 53.1 | 50.2 |
| 145 | 6 | 430 | 9.33 | −0.16 | 0.48 | 4 | 0 | 0.75 | 46.7 | 43.6 |
| 146 | 6 | 430 | 9.33 | −0.16 | 0.48 | 4 | 0 | 1.25 | 42.6 | 39.6 |
| 147 | 6 | 430 | 9.33 | −0.16 | 0.48 | 4 | 0 | 1.75 | 39.3 | 36.3 |
| 148 | 6 | 430 | 9.33 | −0.16 | 0.48 | 4 | 0 | 2.25 | 37.8 | 34.8 |
| 149 | 6 | 430 | 9.33 | −0.16 | 0.48 | 4 | 0.35 | 0 | 57.4 | 55.1 |

(*continued on next page*)

**Table A4** (*continued*)

| Experiment | P, bar | T, °C | $W/F^0_{CO_2}$, g h mol$^{-1}$ | $\varepsilon_A$[a] | $p^{in}_{CO_2}$, bar | H/C[b] | M/C[c] | A/C[d] | $X_{CO_2}$, % | $Y_{CH_4}$, % |
|---|---|---|---|---|---|---|---|---|---|---|
| 150 | 6 | 430 | 9.33 | −0.16 | 0.48 | 4 | 0.70 | 0 | 55.9 | 53.5 |
| 151 | 6 | 430 | 9.33 | −0.16 | 0.48 | 4 | 1.05 | 0 | 55.3 | 52.9 |
| 152 | 6 | 430 | 9.33 | −0.16 | 0.48 | 4 | 1.65 | 0 | 55.1 | 52.6 |
| 153 | 6 | 430 | 9.33 | −0.16 | 0.48 | 4 | 2.05 | 0 | 54.7 | 52.1 |

[a] Extent of reaction defined as: $\varepsilon_A = -2y^{in}_{CO_2}$.
[b] H/C corresponds to $H_2$ to $CO_2$ molar ratio in the feedstream.
[c] M/C corresponds to $CH_4$ to $CO_2$ molar ratio in the feedstream.
[d] A/C corresponds to $H_2O$ to $CO_2$ molar ratio in the feedstream.

$$r_{CH_4} = k_6 \frac{p_{CO}}{K_5} \Theta_* \sqrt{K_1 p_{H_2}} \Theta_* \rightarrow r_{CH_4} = k_6 \frac{\sqrt{K_1}}{K_5} p_{CO} p^{0.5}_{H_2} \Theta^2_* \tag{A3.17}$$

As the active site over which $CH_4$ is formed is assumed to be the same as that for formates decomposition (Ni-$Al_2O_3$ interface), the fraction of free active sites can be considered equal. Then,

$$r_{CH_4} = \frac{k_6 \frac{\sqrt{K_1}}{K_5} p_{CO} p^{0.5}_{H_2}}{\left(1 + \sqrt{K_1 p_{H_2}} + K_2 K_3 p_{CO_2} \sqrt{K_1 p_{H_2}} + \frac{p_{CO}}{K_5} + \frac{p_{H_2O}}{K_{11} K_{12} \sqrt{K_1 p_{H_2}}}\right)^2} \tag{A3.18}$$

Grouping constants similarly and considering equilibrium of CO methanation, the $CH_4$ formation rate results in:

$$r_{CH_4} = \frac{k_6 p_{CO} p^{0.5}_{H_2} \left(1 - \frac{p_{CH_4} p_{H_2O}}{p_{CO} p^3_{H_2} K_{eq3}}\right)}{\left(1 + \sqrt{K_{H_2} p_{H_2}} + K_{CO_2} p_{CO_2} \sqrt{K_{H_2} p_{H_2}} + K_{OH} \frac{p_{H_2O}}{p^{0.5}_{H_2}} + K_{CO} p_{CO}\right)^2} \tag{A3.19}$$

Finally, being CO the only by-product, its formation rate is deduced from different:

$$r_{CO} = (-r_{CO_2}) - r_{CH_4} \tag{A3.20}$$

### *A4 Operational conditions and kinetic data in kinetic measurements*

The partial pressure of reagents ($p_{CO_2}$ and $p_{H_2}$) and products ($p_{CH_4}$, $p_{H_2O}$ and $p_{CO}$) at reactor outlet as a function of parameters defined in Table A4 can be calculated from the following expressions:

$$P^{out}_{CO_2} = P^{in}_{CO_2} \frac{1 - Y_{CH_4} - Y_{CO}}{1 + \varepsilon_A Y_{CH_4}} \tag{A4.1}$$

$$P^{out}_{H_2} = P^{in}_{CO_2} \frac{h - 4Y_{CH_4} - Y_{CO}}{1 + \varepsilon_A Y_{CH_4}} \tag{A4.2}$$

$$P^{out}_{CH_4} = P^{in}_{CO_2} \frac{m + Y_{CH_4}}{1 + \varepsilon_A Y_{CH_4}} \tag{A4.3}$$

$$P^{out}_{H_2O} = P^{in}_{CO_2} \frac{v + 2Y_{CH_4} + Y_{CO}}{1 + \varepsilon_A Y_{CH_4}} \tag{A4.4}$$

$$P^{out}_{CO} = P^{in}_{CO_2} \frac{Y_{CO}}{1 + \varepsilon_A Y_{CH_4}} \tag{A4.5}$$

which are deduced considering that $CH_4$ and CO are formed following the stoichiometry of $CO_2$ methanation ($CO_2 + 4H_2 \rightarrow CH_4 + 2H_2O$) and reverse water gas shift ($CO_2 + H_2 \rightarrow CO + H_2O$) reactions, respectively.

Regarding $CO_2$ conversion is calculated with Eq. (2), whereas yield to methane ($Y_{CH_4}$) is calculated with the Eq. (5).

## Appendix B. Supplementary data

Supplementary material related to this article can be found, in the online version, at doi:https://doi.org/10.1016/j.jcou.2022.101888.

## References


[1] G.H. Rau, J.R. Baird, Renew. Sustain. Energy Rev. 95 (2018) 265–272.
[2] F. Gervais, Earth-Sci. Rev. 155 (2016) 129–135.
[3] M. Child, O. Koskinen, L. Linnanen, C. Breyer, Renew. Sustain. Energy Rev. 91 (2018) 321–334.
[4] P. Sabatier, Comptes Rendus 134 (1902) 514–516.
[5] M. Thema, F. Bauer, M. Sterner, Renew. Sustain. Energy Rev. 112 (2019) 775–787.
[6] X. Zhang, C. Bauer, C.L. Mutel, K. Volkart, Appl. Energy 190 (2017) 326–338.
[7] J. Gao, Y. Wang, Y. Ping, D. Hu, G. Xu, F. Gu, F. Su, RSC Adv. 2 (2012) 2358–2368.
[8] W. Li, H. Wang, X. Jiang, J. Zhu, Z. Liu, X. Guo, C. Song, RSC Adv. 8 (2018) 7651–7669.

[9] B. Alrafei, I. Polaert, A. Ledoux, F. Azzolina-Jury, Catal. Today 346 (2020) 23–33.
[10] A. Bermejo-López, B. Pereda-Ayo, J.A. González-Marcos, J.R. González-Velasco, Appl. Catal. B: Environ. 256 (2019), 117845.
[11] A. Bermejo-López, B. Pereda-Ayo, J.A. González-Marcos, J.R. González-Velasco, J. Co2 Util. 34 (2019) 576–587.
[12] A. Karelovic, P. Ruiz, J. Catal. 301 (2013) 141–153.
[13] M. Mihet, M.D. Lazar, Catal. Today 306 (2018) 294–299.
[14] H.T.T. Nguyen, Y. Kumabe, S. Ueda, K. Kan, M. Ohtani, K. Kobiro, Appl. Catal. A: Gen. 577 (2019) 35–43.
[15] H.H. Shin, L. Lu, Z. Yang, C.J. Kiely, S. McIntosh, ACS Catal. 6 (2016) 2811–2818.
[16] Z. Bian, Y.M. Chan, Y. Yu, S. Kawi, Catal. Today 347 (2020) 31–38.
[17] T.A. Le, T.W. Kim, S.H. Lee, E.D. Park, Catal. Today 303 (2018) 159–167.
[18] J. Tan, J. Wang, Z. Zhang, Z. Ma, L. Wang, Y. Liu, Appl. Surf. Sci. 481 (2019) 1538–1548.
[19] A. Quindimil, U. De-La-Torre, B. Pereda-Ayo, J.A. González-Marcos, J.R. González-Velasco, Appl. Catal. B: Environ. 238 (2018) 393–403.
[20] J.N. Dew, R.R. White, C.M. Sliepcevich, Ind. Eng. Chem. 47 (1955) 140–146.
[21] P.J. Lunde, F.L. Kester, Ind. Eng. Chem. Proc. Des. Dev. 13 (1974) 27–33.
[22] J.H. Chiang, J.R. Hopper, Ind. Eng. Chem. Prod. Res. Dev. 22 (1983) 225–228.
[23] R.E. Hayes, W.J. Thomas, K.E. Hayes, J. Catal. 92 (1985) 312–326.
[24] G.D. Weatherbee, C.H. Bartholomew, J. Catal. 77 (1982) 460–472.
[25] T. Kai, T. Takahashi, S. Furusaki, Can. J. Chem. Eng. 66 (1988) 343–347.
[26] W. Wang, S. Wang, X. Ma, J. Gong, Chem. Soc. Rev. 40 (2011) 3703–3727.
[27] K. Jalama, 59 (2017) 95–164.
[28] A. Westermann, B. Azambre, M.C. Bacariza, I. Graça, M.F. Ribeiro, J.M. Lopes, C. Henriques, Appl. Catal. B: Environ. 174–175 (2015) 120–125.
[29] J.L. Falconer, A.E. Zağli, J. Catal. 62 (1980) 280–285.
[30] P.A.U. Aldana, F. Ocampo, K. Kobl, B. Louis, F. Thibault-Starzyk, M. Daturi, P. Bazin, S. Thomas, A.C. Roger, Catal. Today 215 (2013) 201–207.
[31] A. Solis-Garcia, J.F. Louvier-Hernandez, A. Almendarez-Camarillo, J.C. Fierro-Gonzalez, Appl. Catal. B: Environ. 218 (2017) 611–620.
[32] Z.A. Ibraeva, N.V. Nekrasov, B.S. Gudkov, V.I. Yakerson, Z.T. Beisembaeva, E. Z. Golosman, S.L. Kiperman, Theor. Exp. Chem. 26 (1991) 584–588.
[33] J. Lefebvre, S. Bajohr, T. Kolb, Fuel 239 (2019) 896–904.
[34] A. Loder, M. Siebenhofer, S. Lux, J. Ind. Eng. Chem. 85 (2020) 196–207.
[35] Y. Yu, Y.M. Chan, Z. Bian, F. Song, J. Wang, Q. Zhong, S. Kawi, Int. J. Hydrogen Energy 43 (2018) 15191–15204.
[36] M.S. Duyar, A. Ramachandran, C. Wang, R.J. Farrauto, J. Co2 Util. 12 (2015) 27–33.
[37] L. Falbo, C.G. Visconti, L. Lietti, J. Szanyi, Appl. Catal. B: Environ. 256 (2019), 117791.
[38] X. Wang, Y. Hong, H. Shi, J. Szanyi, J. Catal. 343 (2016) 185–195.
[39] F. Koschany, D. Schlereth, O. Hinrichsen, Appl. Catal. B: Environ. 181 (2016) 504–516.
[40] T. Burger, P. Donaubauer, O. Hinrichsen, Appl. Catal. B: Environ. 282 (2021), 119408.
[41] C.V. Miguel, A. Mendes, L.M. Madeira, J. Co2 Util. 25 (2018) 128–136.
[42] P. Marocco, E.A. Morosanu, E. Giglio, D. Ferrero, C. Mebrahtu, A. Lanzini, S. Abate, S. Bensaid, S. Perathoner, M. Santarelli, R. Pirone, G. Centi, Fuel 225 (2018) 230–242.
[43] I. Champon, A. Bengaouer, A. Chaise, S. Thomas, A. Roger, J. Co2 Util. 34 (2019) 256–265.
[44] A. Cárdenas-Arenas, A. Quindimil, A. Davó-Quiñonero, E. Bailón-García, D. Lozano-Castelló, U. De-La-Torre, B. Pereda-Ayo, J.A. González-Marcos, J. R. González-Velasco, A. Bueno-López, Appl. Catal. B: Environ. 265 (2020), 118538.
[45] A. Quindimil, M.C. Bacariza, J.A. González-Marcos, C. Henriques, J.R. González-Velasco, Appl. Catal. B: Environ. 296 (2021), 120322.
[46] J.I. Di Cosimo, V.K. Díez, M. Xu, E. Iglesia, C.R. Apesteguía, J. Catal. 178 (1998) 499–510.
[47] L. Falbo, M. Martinelli, C.G. Visconti, L. Lietti, C. Bassano, P. Deiana, Appl. Catal. B: Environ. 225 (2018) 354–363.
[48] L. Xu, X. Lian, M. Chen, Y. Cui, F. Wang, W. Li, B. Huang, Int. J. Hydrogen Energy 43 (2018) 17172–17184.
[49] G. Garbarino, C. Wang, T. Cavattoni, E. Finocchio, P. Riani, M. Flytzani-Stephanopoulos, G. Busca, Appl. Catal. B: Environ. 248 (2019) 286–297.
[50] D.E. Mears, Ind. Eng. Chem. Proc. Des. Dev. 10 (1971) 541–547.
[51] J. Anderson, Chem. Eng. Sci. 18 (1963) 147–148.
[52] G. Poncelet, M.A. Centeno, R. Molina, Appl. Catal. A Gen. 288 (2005) 232–242.
[53] D. Förtsch, Energy 205 (2020), 117883.
[54] T.A. Le, J. Kim, J.K. Kang, E.D. Park, Catal. Today 356 (2020) 622–630.
[55] G. Garbarino, D. Bellotti, P. Riani, L. Magistri, G. Busca, Int. J. Hydrogen Energy 40 (2015) 9171–9182.